2006

The effect of porosity on the fatigue life of 8630 cast steel

Paul T Deegan
University of Iowa

THE EFFECT OF POROSITY ON THE FATIGUE LIFE OF 8630 CAST STEEL

by

Paul T. Deegan

A thesis submitted in partial fulfillment
of the requirements for the Master of
Science degree in Mechanical Engineering
in the Graduate College of
The University of Iowa

May 2006

Thesis Supervisor: Professor Ralph I. Stephens

Graduate College
The University of Iowa
Iowa City, Iowa

CERTIFICATE OF APPROVAL

_____

MASTER'S THESIS

_____

This is to certify that the Master's thesis of

Paul T. Deegan

has been approved by the Examining Committee
for the thesis requirement for the Master of Science
degree in Mechanical Engineering at the May 2006 graduation.

Thesis Committee: _____
Ralph I. Stephens, Thesis Supervisor

_____
Christoph Beckermann

_____
Richard Hardin

For My Grandfather: J. Wayne Deegan

TABLE OF CONTENTS

LIST OF TABLES

LIST OF FIGURES

CHAPTER 1: INTRODUCTION

1.1 Background

Cast steels make up a growing part of the steel industry. Advances have made it possible to reach a wide range of consumer demands for cast steel products. However, within the steel foundry industry the total amount of cast steel produced makes up only 2% of the entire steel production. The bulk of the steel industry is devoted to wrought steel that supplies other industries with the raw material needed to form their products. Cast steel, however, is beginning to grow in popularity due to the advances in alloys and the construction of molds. The comprehension of fluid dynamics and heat transfer has also grown in the last decade; this too has led to advances in cast steel production and usage. Cast steel products have become more intricate and specialized, for example in extreme environmental abuse, including high heat, corrosive surroundings, and multiaxial stress. Castings can range from a few ounces to well over a hundred tons [1]. Research has been geared to help understand the physics of casting, and testing has been implemented to validate theories. The better the physics of casting can be understood, more superior castings can be produced, and the industry can continue to grow and fulfill a greater amount of needs.

1.2 Previous Study Review

The research conducted for this thesis is primarily a continuation of previous research done by Kyle Sigl [2] in 2002 in The University of Iowa Fatigue and Fracture Laboratory in conjunction with The University of Iowa Solidification Laboratory. The study that was conducted investigated the influence of porosity in fatigue using AISI 8630 cast steel. The study was designed to fatigue test specimens made from 8630 cast steel with varying levels of porosity, and will be briefly described here. For a complete report on the work the reference material should be used.

Four castings were designed by The University of Iowa Solidification Laboratory. The castings were designed to be sound, and three levels of macroporous specimens: low, medium, and high. The level of macroporosity was confirmed for each specimen using radiography. The specimens were fatigue tested axially using a fully reversed condition, that subjects the specimens to equal magnitudes of maximum and minimum limits. These limits are either stress or strain dependent based on the test method. Monotonic tests were also performed on the specimens from the sound casting to determine monotonic properties. In addition to mechanical testing, fractography and microscopy imaging were conducted on selected specimens. The purpose of the image analysis was to examine the fracture mechanisms involved, and examine the porosity.

Monotonic and fatigue properties were determined for the sound specimens and compared to results found for sound 8630 cast steel conducted for the Steel Founder's Society of America (SFSA) in 1983 [3].The monotonic ultimate strength, S_u, and modulus of elasticity, E, were similar, however, the ductility measured in Sigl's specimens was significantly less than what was measured in the SFSA study. The fatigue properties were also different and showed more than a 50% decrease in fatigue strength, S_f, at $2x10^6$ cycles. The results of the fractography showed ductile dimples in the fracture surface that indicated high energy ductile failure; however the microscopy study revealed microporosity. Microporosity cannot be resolved using radiography so the material appears sound radiographically. The microporosity found in the Sigl's sound specimens was relatively prevalent even though the amount of porosity contained was less than 1%. In the literature review done in his study Sigl found that the existence of microporosity could reduce the ductility of a material, and the fatigue life as well. Based on these findings the material could not be considered sound, but instead was classified as microporous.

Fatigue testing was also performed on the varying levels of macroporous specimens. The fatigue results for these specimens were compared to the results of the

microporous specimens. To have comparable fatigue lives, the stress amplitudes for the macroporous specimens had to be reduced considerably. Since the stress amplitudes were so much lower when they were compared to the microporous specimens they showed no similar trends. Comparing the different levels of macroporous specimens to each other also showed no trends. The different levels of porosity in Sigl's macroporous specimens showed no difference of fatigue life over one another. The fractography showed the amount of macroporosity of some specimens to overwhelm the cross section and make the specimen look like a thin walled tube, while others had a more even dispersion of smaller pores across the cross section. The percentage of the cross section affected by porosity was estimated to be 10-30% on the macroporous specimens using microscopy.

The modulus of elasticity for the macroporous specimens was found to vary significantly for each specimen. Using a ratio of the specimen modulus of elasticity compared to the modulus of elasticity of the microporous specimens, an estimation of porosity was hypothesized. Using this ratio a corrected stress was calculated that was applied to each macroporous specimen. The corrected stress helped to form trends for the specimens based on the measured modulus of elasticity, but did not totally account for the stress reduction found. Additionally the estimation of porosity based on the ratio of modulus of elasticity was not verified by the microscopy techniques.

The results of the study showed that material originally thought to be sound was not, and had an amount of microporosity that reduced the fatigue properties. The macroporous material had porosity that overwhelmed the test section, and the results were not comparable to the microporous specimens or the sound data from the SFSA study. In an extension study done by Sigl et al [4], the data were used for modeling porosity effects in fatigue. He made fatigue life calculations using both strain-life and linear elastic fracture mechanics.

1.3 Thesis Motivation

The objective of this research was to continue the goals set forth by Kyle Sigl and implement the recommendations made at the conclusion of his study. The objective was to investigate further the effects of porosity in 8630 cast steel. Different castings for specimens were designed by the University of Iowa Solidification Laboratory to develop different levels of porosity. These castings had three different geometries which were a truncated cone, a cylinder with a disc, and a straight cylinder. The Truncated cone was designed so that the casting would have a strong temperature gradient, and would minimize any development of porosity. This would serve as sound material that could be compared directly to the sound material tested in the 1983 SFSA study. The cylinder with disc castings were designed to have a hot spot focused where the specimen test section was machined. This hot spot increased the amount of porosity that would form, where it was detected by radiography. These castings had three different cast disc thicknesses of 3, 4, and 5 mm. Based on casting simulations the thickness of the disc was directly related to the formation of macroporosity, an increase of thickness also indicated an increase of macroporosity. The straight cylinder casting was designed to develop porosity along the centerline of the cylinder as evenly as possible. Casting simulations predicted more microporosity formation, but macroporosity would also be present. Specimens machined from these castings were designed to have an increased test section diameter of 9 mm up from the previous study of 5 mm. The increase in diameter resulted in a 223% increase in cross sectional area. Radiography was used to validate the occurrence of macroporosity in all specimens.

Specimens from the truncated cone castings were tested for monotonic and fatigue properties. Fatigue testing was performed using both strain and stress control. The results were then compared to both monotonic and fatigue properties found in the SFSA results from 1983 [3] and the Sigl results from 2002 [2]. The comparison confirmed that a strong temperature gradient could produce sound cast steel relative to a

casting from a keel block. Specimens from cylinder with disc castings and the straight cylinder casting were tested in stress control using the R=-1 condition. Using an S-N (stress-life) method, the macroporosity specimens could be compared to sound material to investigate the effect of porosity in fatigue life. Fractography was conducted on representative specimens to examine the fracture surfaces for mechanisms involved in fatigue crack growth and final fracture. Additional evidence of porosity was also discovered. Grinding back the immediate fracture surface a two-dimensional representative of the porosity could be seen under magnification. The use of microscopy was employed to determine the average size and frequency of occurrence of pores. Key recommendations made by Sigl were to reduce the amount of macroporosity, and increase the size of the macroporosity specimens. Through the use of casting simulation by the University of Iowa Solidification Laboratory both of these recommendations were implemented.

CHAPTER 2: TEST MATERIAL

2.1 Blank Casting

Specimen blanks were cast from AISI 8630 cast steel. The University of Iowa Solidification Laboratory designed a casting pattern with eight blanks cast in five different geometries. The geometries were designed to induce an amount of porosity less than that found in Kyle Sigl's research done in 2002 [2]. A photograph of the casting pattern is shown in Figure 2.1 and shows the blanks lettered A-H. The mold fills from the bottom to each specimen blank, each with a diameter of 25 mm. The molten metal continues to fill vertically to the top where each individual blank had a 72 mm tall riser which was vented. Blank sections A and F were truncated cone shaped to create a strong temperature gradient to minimize the formation of porosity. The height of the truncated cone blank was 133 mm from the start of the taper to the riser, and had a diameter of 52 mm at the top where the riser began. Blank sections B and G were straight cylinders with a height of 158 mm and a diameter of 25 mm. The straight cylinder was predicted to produce porosity along the centerline of the blank; however the initial simulation did not predict any. The blanks cast for C, D, E, and H were all cylindrical specimens with a flat disc cast halfway up the length. The dimensions of the blanks were identical to that of the straight cylinder with the exception of the 52 mm diameter disc with varying thicknesses. This disc was to generate porosity by inducing a hot spot around its location which cooled at slower rate than the surroundings. The difference between the specimen blanks was the thickness of the discs. The C blank had a 5 mm thick disc, the D blank had a 4 mm disc, and the E and H blanks had 3 mm discs. With the increase of the disc thickness the hot spots persist longer therefore increasing the amount of porosity that would form. A three-dimensional computer generated model of the resulting casting is shown in Figure 2.2.

Ten molds were formed from a no-bake chemical sand called Pepset. The castings were poured at Southern Cast Products in Meridian, Mississippi where heat treatment also took place. After casting, the blanks were normalized at 900ºC, then austenized at 885ºC, water quenched, and tempered at 510ºC for 1.5 hours. Two separate truncated cone specimens were used to measure the machined specimen hardness that was performed at the University of Iowa Material Science Lab. Ends of the grip section were cut then ground flat using a rotating disc sanding machine. Preparation and testing of the specimen cross section for hardness testing was done in accordance with ASTM standard E18 [5]. Five separate tests were taken across the face of each specimen and averaged which yielded a value of 36 Rockwell C. This method tested the internal hardness and not the surface of the specimen. The final chemical composition was 1.06% manganese, 0.82% chromium, 0.57% nickel, 0.38% silicone, 0.31% molybdenum, 0.28% carbon, 0.010% phosphorus, and 0.007% sulfur. A comparison to Kyle Sigl's research [2] and the SFSA study [3] are shown in Table 2.1. The quantities found are close to the standards set forth by the Steel Casting Handbook [6] for wrought AISI 8630 steel. Some elements such as silicone are increased to aid in fluidity for casting, while some elements are incidental, such as nickel, chromium, and molybdenum, and can exceed the recommended chemistry by a certain amount. The chemistry reported falls within these specifications.

2.2 Specimen Design

The specimen dimensions were based on ASTM standard E606 [7] that sets standards for strain controlled testing. These standards are also compatible for load controlled testing as well. The University of Iowa Solidification Laboratory designed molds where AISI 8630 cast steel would form the blanks from which the test specimens were machined. As indicated in section 2.1, the blanks had three distinctive shapes to induce varying types of porosity predicted by the laboratory; a truncated cone, a cylinder

with a disc, and a straight cylinder. The truncated cone blank model predicted a sound casting with little or no porosity due to its strong temperature gradient. The straight cylinder model predicted centerline porosity throughout the length of the blank. The cylinder with disc models predicted the porosity to develop around the disc about the centerline. The disc seemed to focus the porosity locally around it in the model and also predicted the pore size to be greater than that of the straight cylinder blank.

From previous testing conducted by Kyle Sigl [2], the porosity on certain specimens overwhelmed the specimen. The ratio of porosity to cross sectional testing area was too large and testing was compromised. In order to reduce this effect a larger specimen was deemed necessary for this research. Based on the dimensions of the cast blanks, the machined specimens were optimized to have the greatest cross sectional area possible while maintaining the standard set forth by ASTM E606. The blanks were shipped to MetCut Research of Cincinnati, Ohio for machining and polishing with the following specifications. The gage diameter for the reduced test section was set at 9 mm; the previous testing used a diameter of 5 mm, resulting in a cross sectional area gain of 223%. The length of the reduced test section was 18 mm which would accommodate the 12.5 mm extensometer. Figure 2.3 shows a view of the cylindrical specimen with dimensions in mm. The specimens were cut from the base of the taper on the truncated cones, while the cylinders with disc specimens were centered about the disc. The straight cylinder specimens were also machined from the center of the blank. Figure 2.4 shows the three different blank geometries and the location where the test specimens were machined. All specimens for identification were engraved with their lettered location in the mold, and which mold it came from.

During machining it was noted that some of the specimens had longitudinal cracks but these did not affect the process of completing the machining. Since the cracks were along the longitudinal axis of the specimen and primarily in the grip regions, it was determined that they theoretically should not affect the testing results. The cause of the

cracks was determined to be from water quenching that occurred during the heat treatment after casting. Similar heat treatment had been done to the previous castings of Kyle Sigl, but had not affected those specimens. The decision was made to continue with the original plan and determine through testing if the cracks had any detrimental influence.

The test section after machining was polished by MetCut to a surface roughness of less than 0.2 microns with the direction of the final scratches going longitudinally. The specimens were then individually packed and shipped to the University of Iowa Fatigue and Fracture Laboratory. Upon arrival each specimen was inspected visually for cracks and the results were recorded with respect to their numbers and locations. Section 2.4 details these observations and effects.

2.3 Radiography

For inspection of macroporosity the machined specimens were taken to Alloyweld of Chicago, Illinois to conduct radiography. As shown in previous research by Kyle Sigl, radiography is a proven method to find macroporosity in steel. There is a limit to the resolution which is determined by the section thickness, and generally pores cannot be resolved that are less than 2% of the section thickness. Based on the thickest part of the test section of 9 mm the smallest pore resolved would be around 200 microns, and anything smaller would be considered microporosity. Specimens were subjected to x-rays while on top of a film that is then developed. The radiography was performed according to ASTM standard E1030 [8]. All specimens were radiographed four times; each view rotated 45º clockwise from the previous. This allowed for a possible three-dimensional reconstruction of the macroporosity in each specimen by the Solidification Laboratory. Through inspection of the radiographs, larger diameter porosity or a high density of pores could be viewed in the specimens as dark regions. Results of radiographs were analyzed to determine the severity of the macroporosity. Figure 2.5 shows representative specimen

test sections radiographs from the truncated cone blanks, it can be seen that there is no evidence of macroporosity in any of the specimen areas. Figure 2.6 shows representative specimen test sections from the cylinder with 3 and 4 mm discs blanks. Some specimens from this group have porosity ranging from none to clear evidence in the fillet region, and small amounts in the test section. The 5 mm blank specimens showed distinct regions of porosity within the fillet region and test sections as shown in Figure 2.7. The straight cylinder blank specimens showed macroporosity throughout the test section shown in Figure 2.8. Generally for the disc specimens macroporosity was observed toward the fillet regions, but in the 5 mm blank specimens it often extended to the test section. Even though some specimens showed no macroporosity, microporosity could still be present. Ultimately this information was used to group the specimens into similar categories. The radiographs for all specimens with the applicable fracture zones are available from the University of Iowa Solidification Lab report upon request.

2.4 Quench Cracks in Specimens

A problem was noticed during the machining of the specimens by the machining company MetCut. It was noticed that several of the specimens had longitudinal cracks that started in the grip section of the specimen and occasionally extended to the test section. Since machining had started and some of the specimens were unaffected the decision was made to continue and inspect the specimens when they were returned. Upon arrival a visual inspection was made of each specimen cataloguing the extent of the cracks and their locations. Figure 2.9 shows radiographic evidence of a cracked specimen.

All groups of blanks were affected, however the different casting geometries showed different crack defects. All but one of the 5 mm disc blank specimens had cracks; two had cracks that extended to the beginning of the test section, while four had at least two cracks. From the 4 mm disc blank specimen only three were unaffected. The

remaining four had single cracks, with one specimen that had a crack extending from end to end through the test section. The 3 mm disc blank group had seven affected specimens, all of which were single cracks. Five of these cracks extended into the beginning of the test section. From the truncated cone specimens only one was affected. It had a single crack but did not extend into the test section. The probable cause of the cracking was determined to be quench cracking in water. It was proposed that since the cracks ran longitudinally they theoretically should not affect axial testing, but a plan to test visually cracked specimens from the same blank group against visually sound specimens was implemented. Four specimen pairs from the same group were tested in load control for long lives with no appreciable difference; in fact the quench cracked specimens had longer lives than visually sound ones in three out of the four tests. From these results it was determined that the quench cracking had a negligible effect on the fatigue life. The results from this testing were incorporated directly into the data pool and used.

Table 2.1 – Cast Steel Chemistry: Percent by Weight

Element	Deegan (2006)	Sigl (2002)	SFSA (1983)
Mn	1.06	0.93	0.84
Cr	0.82	0.48	0.51
Ni	0.57	0.50	0.61
Si	0.38	0.66	0.53
Mo	0.31	0.27	0.17
C	0.28	0.29	0.30
S	0.007	0.022	0.022
P	0.010	0.027	0.021

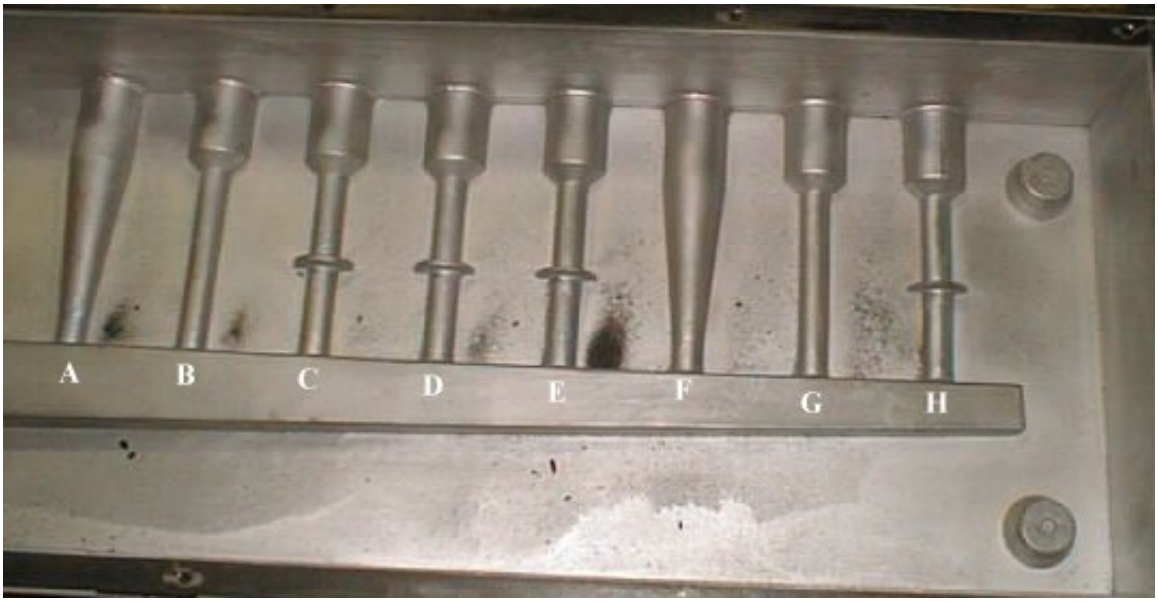

Figure 2.1 - Photograph of Pattern with Individually Labeled Blanks

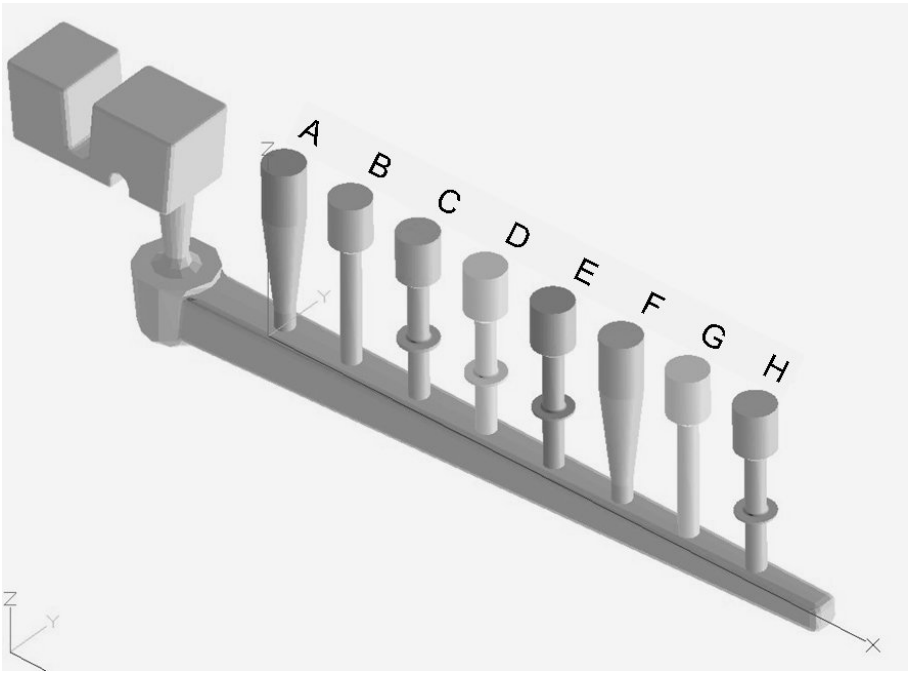

Figure 2.2 - Three Dimensional Model of Casting with Individually Labeled Blanks

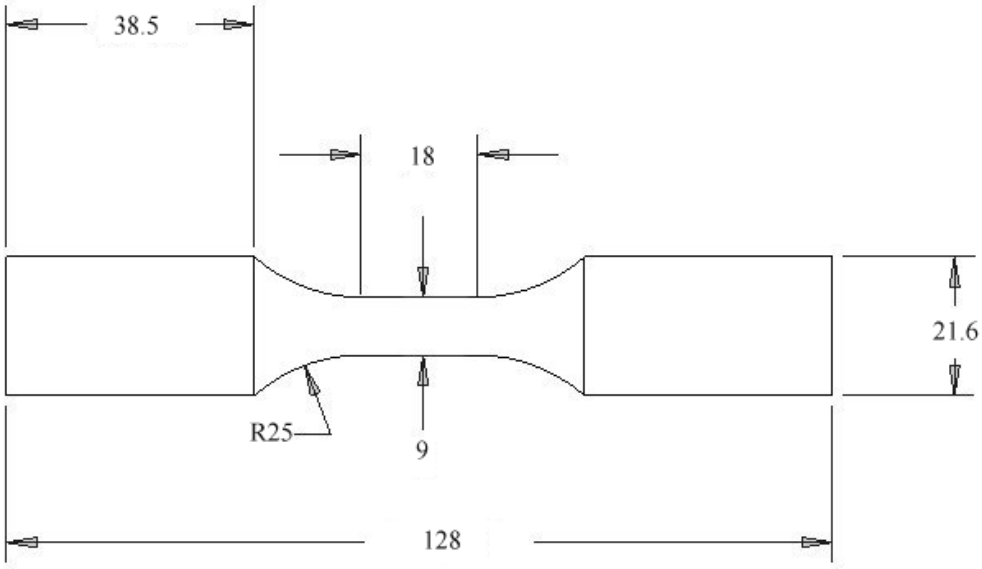

Figure 2.3 - Cylindrical Test Specimen with Dimensions in mm

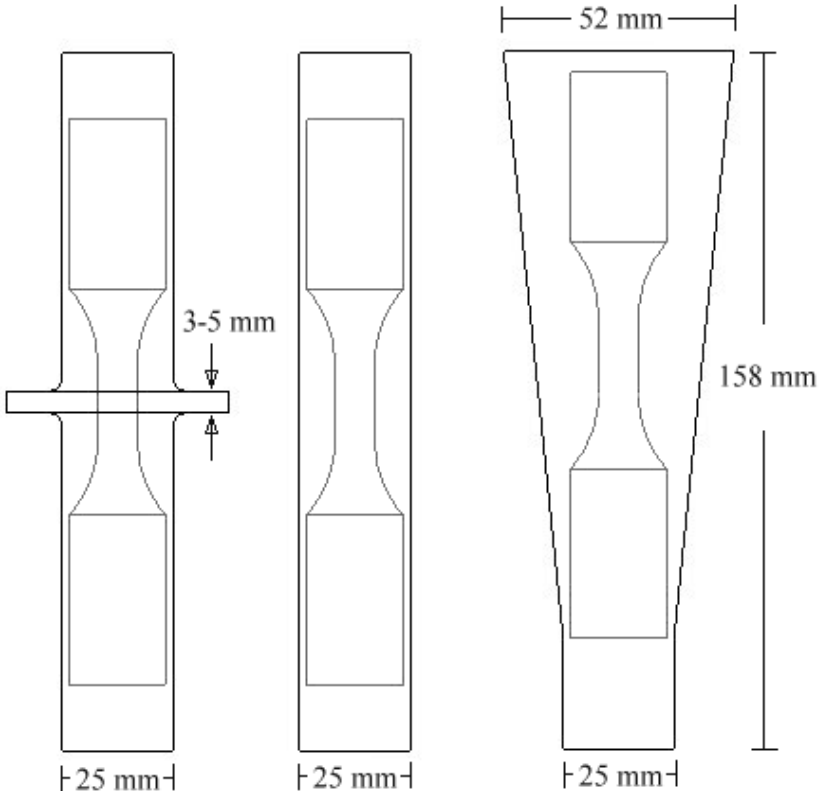

Figure 2.4 - Specimen Locations with Respect to Cast Blank Geometry

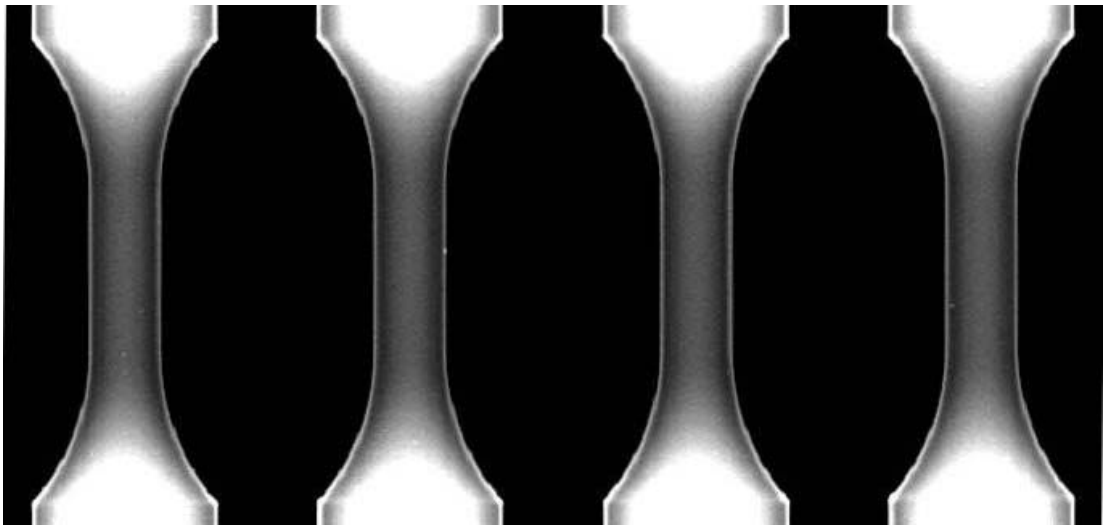

Figure 2.5 - Representative Radiographs of Truncated Cone Specimens

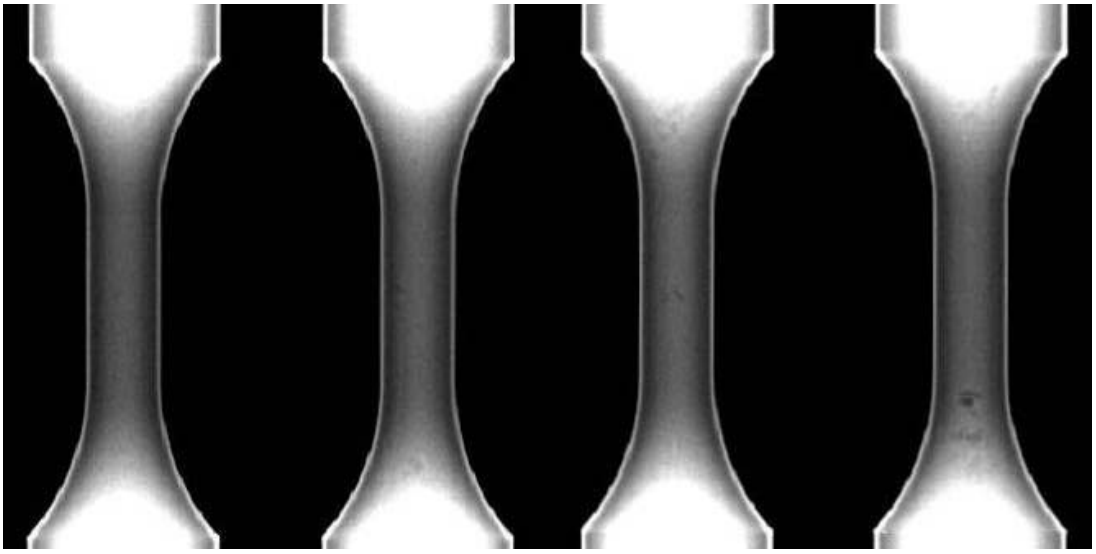

Figure 2.6 - Representative Radiographs of Cylinder with 3 and 4 mm Disc Specimens

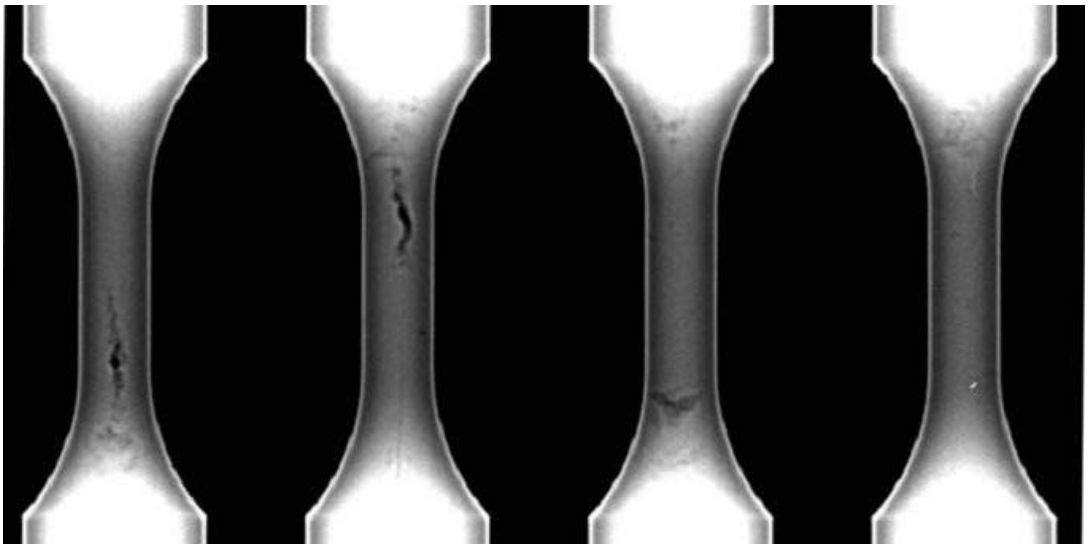

Figure 2.7 - Representative Radiographs of Cylinder with 5 mm Disc Specimens

Figure 2.8 - Representative Radiographs of Straight Cylinder Specimens

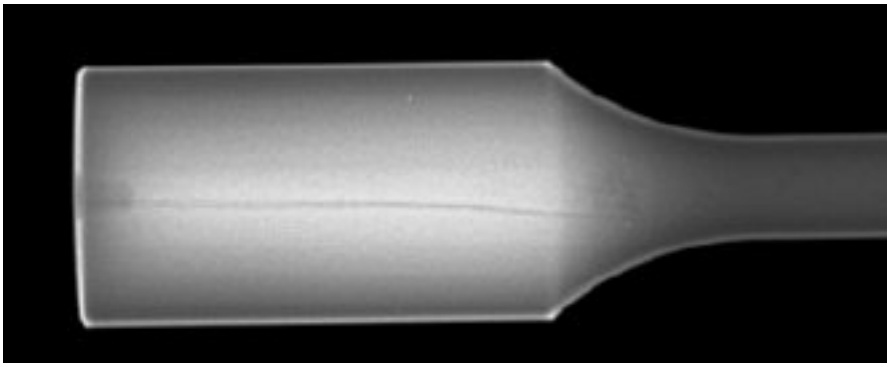

Figure 2.9 - Radiographic Image of Quench Crack in Grip Section

CHAPTER 3: TESTING METHODS

3.1 Testing Equipment

Testing was conducted using an MTS 810 closed loop servo-hydraulic load frame that was controlled by a TestStar II controller. TestStar II software installed on a Dell personal computer with a 266 MHz Pentium II processor was used to set up testing using TestWareSX and 790.20 Fatigue Test Application software, that are all part of the TestStar family. The specimens were gripped using MTS 647 hydraulic V-notched wedge grips with inserts designed for diameters 17-22.9 mm. The system was set to grip with ~15 MPa of pressure that made indentations into the specimen grip sections, but did not affect testing or the reduced test section. Data were collected by an MTS 661.2E-03 load cell and 632.13B-20 extensometer; both were calibrated by an MTS field service engineer on June 29, 2004. The load cell was attached between the load frame and the upper grip while the lower grip was driven axially by the hydraulic ram. The extensometer was attached to the reduced test section of the specimen using orthodontic rubber bands which held the extensometer blades into two separate bands of cellophane tape. Two layers of tape were used to eliminate contact with the knife edges that could lead to a stress concentration at that point, during fatigue testing.

For monotonic tests, a constant rate of ram displacement was used to create tension until the specimen fractured. Using TestWareSX, a test was set up to record strain from the extensometer, displacement from the load frame ram, and force from the load cell. These tests were used to determine the monotonic properties yield and ultimate strengths (S_{yt}, S_{ut}), percent reduction of area (%RA), and the modulus of elasticity (E).

Fatigue tests were conducted using 790.20 Fatigue Testing Application. All tests were conducted in a fully reversed, R=-1 condition. R in strain control is defined by Equation 3.1 where ε_{min} and ε_{max} are the limits of the strain range. Under load control R is

defined by Equation 3.2 and σ_{min} and σ_{max} are the limits of the stress range based on the nominal cross sectional area of the specimen test section.

$$R = \frac{\varepsilon_{min}}{\varepsilon_{max}} \tag{3.1}$$

$$R = \frac{\sigma_{min}}{\sigma_{max}} \tag{3.2}$$

Under conditions where the specimen underwent plastic deformation, the tests were conducted under constant strain amplitude. Using the Low Cycle Fatigue (LCF) setting in the software, the hydraulic ram operated in a triangular waveform based on the feedback from the extensometer to meet the strain criteria set. The cycling frequencies had to be kept less than 1 Hz in order insure the end levels of the test would be met. The test terminated once the specimen fractured or a drop in load of more than 75% had occurred. If the strain amplitude was determined to be predominantly elastic, then the testing was accomplished using load control. By using feedback from the load cell, the ram operated to apply specified loads. The loads specified were calculated from the stress based on the nominal cross sectional area of the specimen. Since the strain levels were lower under elastic deformation, the tests were run using a sinusoidal wave from the High Cycle Fatigue (HCF) setting in the 790.20 Fatigue Testing Application. Cycling frequencies were increased to 3-18 Hz, and the load end levels were still accomplished. Test termination occurred when the specimen fractured.

3.2 Truncated Cone Testing

Monotonic tests were conducted on two specimens to obtain monotonic properties and to compare the monotonic properties to previous benchmark data. The tests were conducted using a constant displacement rate until the specimen fractured. Based on the

increased cross sectional area of the specimen compared to previous testing by Kyle Sigl [2], a displacement rate of 0.1 mm/s was chosen because it was lower. For the subsequent test, the displacement rate was increased to 0.3 mm/s. The extensometer was attached at the center of the specimen gage length, but the specimen strain went beyond the 3% limit set before fracture. However using displacement data in conjunction with stress data it was possible to determine the monotonic properties.

Twelve truncated cone specimens were used to construct stress-life (S-N) and strain-life (ε-N) fatigue curves. By combining all the specimens from the group, the fatigue properties were calculated. Starting at 0.01 strain amplitude, the testing decreased in amplitude using LCF. All tests were conducted at 0.25Hz while the amplitude was decreased to 0.008, 0.006, 0.005, 0.004, and finally 0.0035 for different specimens. The cyclic stress-strain data were analyzed after each test and at a strain amplitude of 0.0035 it was determined that the deformation was almost entirely elastic. Additionally one specimen, A8, was tested in strain control using an incremental method to determine cyclic stress-strain behavior. This method cycles the specimen at a specific strain amplitude until a steady load is achieved, then the amplitude is increased. The strain amplitudes for this specimen were 0.0035, 0.004, 0.005, and 0.006. After increasing the strain amplitude to 0.008 the specimen load continued to drop and a crack was noticed. The data obtained from this single test was used to compliment the cyclic stress-strain properties gained from the companion method. The companion method uses the multiple fatigue specimens where each specimen is tested at single stress/strain amplitudes until failure. Then representative stress and strain data were used from each specimen to determine the cyclic stress-strain properties.

The testing was then switched to HCF using load control so that the frequency could be increased. The same decrease in strain amplitude (ε_a) defined in Equation 3.3 started in LCF testing was continued in HCF testing. This was accomplished by

calculating the alternating stress (σ_a) based on the nominal cross sectional area divided by the average modulus of elasticity (E) from the monotonic tests.

$$\varepsilon_a = \frac{\sigma_a}{E} \tag{3.3}$$

The first HCF specimen was started at the amplitude of 587 MPa that corresponds to a strain amplitude of 0.003. The predetermined run-out value of $2x10^6$ cycles was achieved at a stress amplitude of 197 MPa that corresponds to a calculated strain amplitude of 0.001. The stress amplitude was stepped down from 587 to 197 MPa at calculated intervals equal to strain amplitudes of 0.005 for each subsequent specimen. The frequency also increased from the initial rate of 3Hz with the final specimen running at 15Hz.

3.3 Cylinder with Disc Specimen Testing

Thirty specimens machined from the cylinders with a disc blank were designed to have macroporosity. The main interest was to investigate the long life fatigue behavior of these specimens, and it was predicted that the lives would be shorter than the truncated cone specimens due to porosity. For comparison to the truncated cone specimens three lower stress levels of 587, 394, and 196 MPa were chosen to begin testing. These correspond to the truncated cone specimen stress amplitudes where the lowest level was the run-out level. All tests were set up in HCF with identical frequencies as the truncated cone counterparts. Stresses lower than 196 MPa did not have to be used, because the specimens achieved the run-out criteria of $2x10^6$ cycles at that level. Multiple specimens were tested at the previously mentioned stress levels for replication of results, with at least two specimens at each amplitude.

3.4 Straight Cylinder Specimen Testing

Ten specimens were machined from the straight cylinder blanks. Identical testing procedure to the cylinder with disc specimens were used on the specimens machined

from the straight cylinder blanks, however run-out did not occur at the previous stress level of 196 MPa. Testing continued at two lower stress levels of 147 MPa and 127 MPa where the lower level achieved the run-out criteria of $2x10^6$ cycles. Two specimens were tested at each level for duplication purposes. Stresses again were calculated based on the nominal cross sectional area of the specimen test section.

CHAPTER 4: EXPERIMENTAL RESULTS

4.1 Monotonic Material Properties

Monotonic material properties were obtained by using two truncated cone blank specimens. Results are shown in Table 4.1 with comparison to the benchmark values found in 1983 [3] and Kyle Sigl's work done in 2002 [2]. It was ultimately determined that Sigl's specimens used for monotonic results were not sound, but contained amounts of microporosity that may have affected the properties. Figure 4.1 shows the stress versus ram displacement for the two monotonic specimens. The average yield and ultimate strengths in tension ($S_{yt,}$ S_{ut}) were found to be 1124 MPa and 1183 MPa respectively for the truncated cones. The S_{ut} average values for all data sets were virtually the same, however S_{yt} for the current data set was slightly higher than the SFSA data that was found using the 0.2% offset method. For each test both truncated cone specimens showed necking before failure with considerable plastic deformation that is reflected in the average percent reduction of area (%RA) of 13. The %RA found from in the 1983 keel block specimens is greater than the new data obtained; this difference could be accounted for due to the yield strength difference from material differences. Figure 4.2 shows a stress-strain relationship of the two monotonic specimens up to 2.5%. By taking a linear regression of the elastic part of the curve the modulus of elasticity (E) was found to be an average of 196 GPa which was close to the previous research. The fracture of the specimens went beyond 3% that was the limit set for the extensometer, and the 2.5% limit shown in Figure 4.2. Thus, the true stress-strain (σ-ε) data could not be obtained to determine the Ramberg-Osgood relationship.

4.2 Truncated Cone Blank Fatigue Material Properties

Thirteen specimens machined from the truncated cone blanks were used to develop the fatigue properties that were compared to sound material from the 1983 SFSA results [3]. The results can be found in Table 4.2 with comparison to the 1983 results [3]

and Kyle Sigl's microporous specimens [2]. The fatigue strength (S_f) at $2x10^6$ cycles of 208 MPa is lower than the 1983 property of 293 MPa, but higher than Sigl's value of 126 MPa, both found at $5x10^6$ cycles. Both Sigl's study and the SFSA study take their S_f value at the run-out value of $5x10^6$ cycles, but analysis of the data shows that no specimens failed between $1x10^6$ and $5x10^6$ cycles. This indicates that the value taken from the current study at $2x10^6$ cycles would be directly comparable to the run-out values from the two previous studies. Figure 4.2 shows the cyclic stress-strain behavior with comparison to the monotonic properties. The cyclic stress-strain curve was developed using data from both the companion and incremental methods. For tests conducted in low cycle fatigue the strain amplitude was held constant for each specimen. This allowed the stress to vary for cyclic softening or hardening, or as cracking developed and the specimen fractured. A stress was needed from the tests so a single cycle was chosen as a representative. The ASTM standard E606 [7] suggests using an approximate half-life for determining stress in strain control testing; however in this case at the approximate half-life point the specimen might not show a valid representation of the behavior. In order to find a steady state behavior for a specimen a variation of the standard was used. This was accomplished using the relationship of stress amplitude to normalized life which is shown in Figure 4.3. During the first cycles the specimen cyclic softens or hardens, while during the final cycles the stress drops significantly which indicate cracking before failure. A quasi-steady state appears in the initial third of the fatigue life before cracking develops, but the stress for higher strain amplitudes of 0.01, 0.008, 0.006, and 0.005 never has a steady load applied for a significant part of the life. The approximate halfway point on quasi-steady state was chosen for representative stress data. Figure 4.4 shows the representative stress-strain hysteresis loops from the four greatest strain amplitude specimens used in the companion method. To augment the cyclic stress-strain results a single specimen, A8, was tested in strain control incrementally at increasing strain amplitudes of 0.0035, 0.004, 0.005, and 0.006. The stress-strain results from this

specimen at steady state have been incorporated with the strain control specimens conducted in the companion testing. The hysteresis loops of the three greatest strain amplitude tests are shown in Figure 4.5 for the incremental method.

For each specimen a hysteresis cycle, as described previously, of the total strain can be broken into two components; the plastic and elastic components as shown in Figure 4.6. The elastic component is found using the peak strain values in compression and tension when unloaded to zero stress. Using these data the plastic component is found by subtracting the total strain from the elastic components. The amount of strain induced in these tests is below 2%. The values can be assumed to be true stress and strain (σ, ε) because the difference is negligible between the engineering values and the true values based on the instantaneous cross-sectional area. By plotting the stress amplitude versus plastic strain amplitude of the companion and incremental specimens, a power law best fit line regression was used to determine the cyclic strength coefficient (K') and strain hardening exponent (n'). This can be defined in equation 4.1:

$$\sigma_a = K' \left(\frac{\Delta \varepsilon_p}{2} \right)^{n'} \tag{4.1}$$

These values are somewhat similar when compared to the 1983 findings. Using total elastic and plastic strain amplitudes ε-N curves were constructed using the 12 fatigue specimens. The test results for these specimens are found in Table 4.3. Equation 4.2 uses the elastic strain amplitude ($\Delta\varepsilon_e/2$) with the monotonic modulus of elasticity (E) versus the reversals to failure ($2N_f$) to determine fatigue strength coefficient (σ_f'), and fatigue strength exponent (b) using a best fit a power law regression line.

$$\frac{\Delta \varepsilon_e}{2} = \frac{\sigma_f'}{E} (2N_f)^b \tag{4.2}$$

The fatigue ductility coefficient (ε_f') and fatigue ductility exponent (c) are found in the same manner using the plastic strain amplitude ($\Delta\varepsilon_p/2$) from in equation 4.3:

$$\frac{\Delta\varepsilon_p}{2} = \varepsilon_f'(2N_f)^c \tag{4.3}$$

The combination of these two curves is used to reconstruct the total strain-life behavior of the truncated cone specimens as shown in Figure 4.7. A comparison of the total stain-life behavior of the truncated cone blank specimens with keel block specimens and Kyle Sigl's microporous specimens is shown in Figure 4.8. Power law line regression can be applied using stress amplitude (S_a) versus cycles to failure (N_f) to create a stress-life (S-N) curve. This is shown in Figure 4.9 with the trend line characterized as a Basquin equation as seen below in equation 4.4. A and B are line fit parameters and the values can be found in Figure 4.9.

$$S_a = A(N_f)^B \tag{4.4}$$

Verification for the stress-life line fit can be done using the strain-life properties. The alternating stress (σ_a) is a function of the fatigue strength coefficient (σ_f'), fatigue strength exponent (b), and the reversals to failure (N_f) and is defined in Equation 4.5.

$$\sigma_a = \sigma_f'(2N_f)^b \tag{4.5}$$

$A = 2^b\sigma_f'$ and $b=B$ theoretically. Upon doing the comparison a plot of the values show very similar lines.

4.3 Cylindrical Blank Specimen Fatigue Testing Results

Specimens machined from cylindrical blanks were divided into three categories based on their original geometry and radiographic results. Blanks with a disc located at the center were categorized by the amount of porosity shown radiographically. A 5 mm disc generally showed more macroporosity while a 3 or 4 mm disc showed less, therefore the 5 mm disc blanks made up a single group and the 3-4 mm disc blank were combined to form another group. The third group consisted of cylindrical blanks without a disc. All groups were tested in load control at similar R=-1 alternating stress levels based on the nominal cross sectional area. One 5 mm disc specimen was tested at a higher level under

load control for quench crack effects and is also included in the results. During testing three specimens failed in the fillet section, therefore these specimen test results are given in Tables 4.5 and 4.6 but not used in calculating fatigue properties or shown in Figure 4.9 trend lines. Test results for the specimens based on the cast blank geometry are found in Tables 4.4, 4.5, 4.6, and 4.7 for 5, 4, 3 mm, and no disc respectively. Using an S-N relationship the individual specimens are plotted and superimposed on the S-N curve for the truncated cone specimens shown in Figure 4.10. Seven specimens machined from the cylinder with disc blank, and two specimens machined from the straight cylinder blank achieved the run-out criterion of $2x10^6$ cycles. A comparison of Sigl's results for both microporous and macroporous specimens to the current research results are shown in Figure 4.11. All strain data for load control testing (HCF) are taken from an approximate half-life cycle of each specimen. Additionally a linear regression was taken assuming totally elastic behavior on the unloading of tension to a zero load. From this regression an unloading modulus of elasticity can be found that represents the particular specimen. The individual moduli are taken from the approximate half-life and are listed in Tables 4.3-4.6 for each specimen. The mean and median of the modulus elasticity along with the standard deviation for each of the cast blank geometries are given in Table 4.8.

Table 4.1 - Truncated Cone/Sound 8630 Steel Monotonic Properties

Property	Specimen A3	Specimen F6	Avg	Sigl (Microporous) [2]	SFSA Paper [3]
S_u (MPa)	1 109	1 258	1 183	1 125	1 144
S_y (MPa)	1 048	1 200	1 124	1 088	985
E (GPa)	197	195	196	197	207
%RA	18	8	13	7	29

Table 4.2 - Truncated Cone/Sound Specimen 8630 Steel Cyclic and Fatigue Properties

Property	Truncated Cones	Sigl (Microporous) [2]	SFSA Paper [3]
S_f (MPa)	208	126	293
S_f/S_u	0.18	0.11	0.26
K´ (MPa)	1 842*	2 550	1 502 / 2 267[#]
n´	0.122*	0.167	0.122 / 0.195[#]
S_y´ (MPa)	840	894	682 / 661[#]
b	-0.185	-0.176	-0.121
c	-0.801	-0.908	-0.693
σ_f´(MPa)	3 214	2 390	1 936
ε_f´	0.23	0.11	0.42

[#]data determined from the companion and incremental step methods respectively

*data combined from the companion and incremental step methods

Table 4.3 – Truncated Cone Fatigue Test Data

Specimen	Frequency (Hz)	σ_a (MPa)	ε_a	N_f	E^d (GPa)
A10	0.25	924[c]	0.0100	100	180
A9	0.25	843[c]	0.0080	230	183
F3	0.25	890[c]	0.0060	493	199
F4	0.25	857[c]	0.0050	594	203
A4	0.25	667[c]	0.0040	1 679	187
A5	0.25	652[c]	0.0035	13 269	198
A6	3	587	0.0030[d]	9 585	206
F5	5	492	0.0024[d]	24 595	209
F8	10	394	0.0019[d]	62 679	207
F9	10	295	0.0015[d]	157 497	206
A7	15	197	0.0010[d]	775 456	206
F10	15	197	0.0010[d]	Run-out[b]	209

[b] Run-out occurs at 2 000 000 cycles

[c] Stress from midpoint cycle of quasi-steady state

[d] Modulus of Elasticity and Strain from approximate ½ life cycle

Table 4.4 - Cylinder with 5 mm Disc Blank Fatigue Test Data

Specimen	Frequency (Hz)	σ_a (MPa)	ε_a [d]	N_f	E^d (GPa)
C10	3	700	0.0036	2 188	203
C3	5	588	0.0030	9 584	201
C4	5	588	0.0030	7 791	202
C5	10	392	0.0020	11 916	210
C6	10	392	0.0020	42 769	200
C9	10	392	0.0020	55 079	199
C7	15	196	0.0010	Run-out*	203
C8	15	196	0.0010	Run-out*	205

* Run-out occurs at 2 000 000 cycles

[d] Modulus of Elasticity and Strain from approximate ½ life cycle

Table 4.5 - Cylinder with 4 mm Disc Blank Fatigue Test Data

Specimen	Frequency (Hz)	σ_a (MPa)	ε_a [d]	N_f	E^d (GPa)
D3	5	588	0.0030	12 144	197
D4[a]	5	588	0.0030	2 178	210
D8	5	588	0.0030	9 375	201
D6	10	400	0.0020	25 435	203
D9	10	400	0.0020	23 741	203
D10	10	392	0.0020	63 593	202
D5	15	196	0.0010	Run-out[b]	208
D7	15	196	0.0010	Run-out[b]	207

[a] specimen failed in fillet section, data not used

[b] Run-out occurs at 2 000 000 cycles

[d] Modulus of Elasticity and Strain from approximate ½ life cycle

Table 4.6 - Cylinder with 3 mm Disc Blank Fatigue Test Data

Specimen	Frequency (Hz)	σ_a (MPa)	ε_a [d]	N_f	E^d (GPa)
E3	5	588	0.0030	17 053	201
E4	5	588	0.0030	11 212	198
E7	5	599	0.0030	10 480	203
H9	5	588	0.0030	6 525	204
H10	5	588	0.0030	10 875	200
E5	10	392	0.0020	59 843	204
E6	10	392	0.0020	116 804	204
E8	10	392	0.0020	38 010	200
H4[a]	10	392	0.0020	57 802	200
H5[a]	10	392	0.0020	58 800	201
H7	15	200	0.0010	18 7742	208
E9	15	200	0.0010	Run-out[b]	206
E10	15	196	0.0010	Run-out[b]	206
H3	15	196	0.0010	Run-out[b]	206

[a] specimen failed in fillet section, data not used

[b]Run-out occurs at 2 000 000 cycles

[d] Modulus of Elasticity and Strain from approximate ½ life cycle

Table 4.7 - Straight Cylinder Blank Fatigue Test Data

Specimen	Frequency (Hz)	σ_a (MPa)	ε_a [d]	N_f	E^d (GPa)
G3	5	588	0.0030	386	191
G5	5	588	0.0030	1 143	173
G10	10	392	0.0020	4 456	186
G7	10	392	0.0020	7 567	172
B1	15	196	0.0010	125 614	203
B7	15	196	0.0010	353 278	195
G1	15	147	0.00075	168 047	211
G4	15	147	0.00075	821 720	202
G8	18	127	0.00065	Run-out[b]	205
G9	18	127	0.00065	Run-out[b]	199

[b]Run-out occurs at 2 000 000 cycles

[d] Modulus of Elasticity and Strain from approximate ½ life cycle

Table 4.8 - Statistical Results of Group Modulus of Elasticity, E, from approximate ½ life

Blank Type	Mean (GPa)	Median (GPa)	Std. Dev. (GPa)
Sound*	199	201	9.6
5mm Disc	203	203	3.6
4mm Disc	204	203	4.3
3mm Disc	203	203	3.0
Straight Cylinder	194	197	13.2

* includes monotonic tests

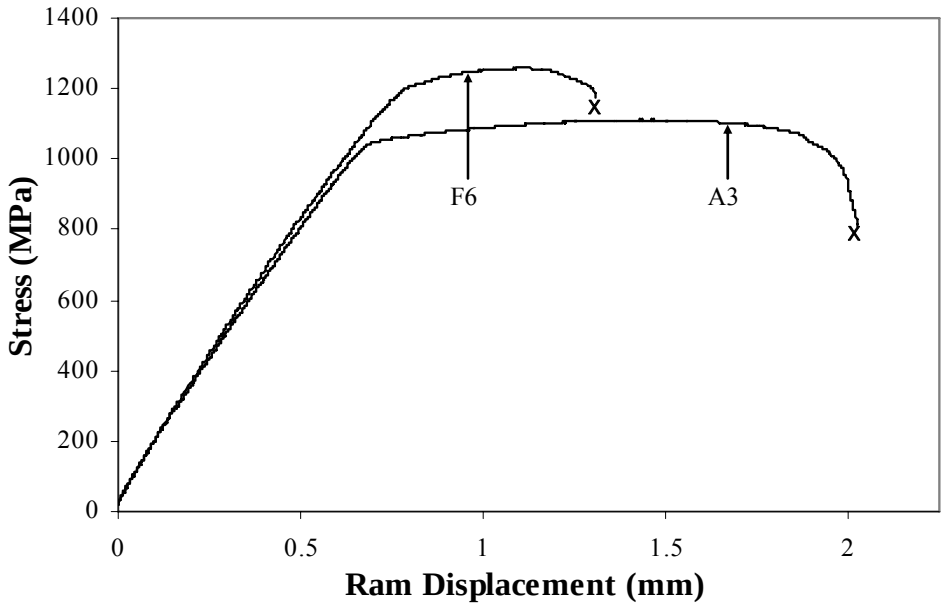

Figure 4.1 - Monotonic Stress-Ram Displacement Curve of Truncated Cone Specimens

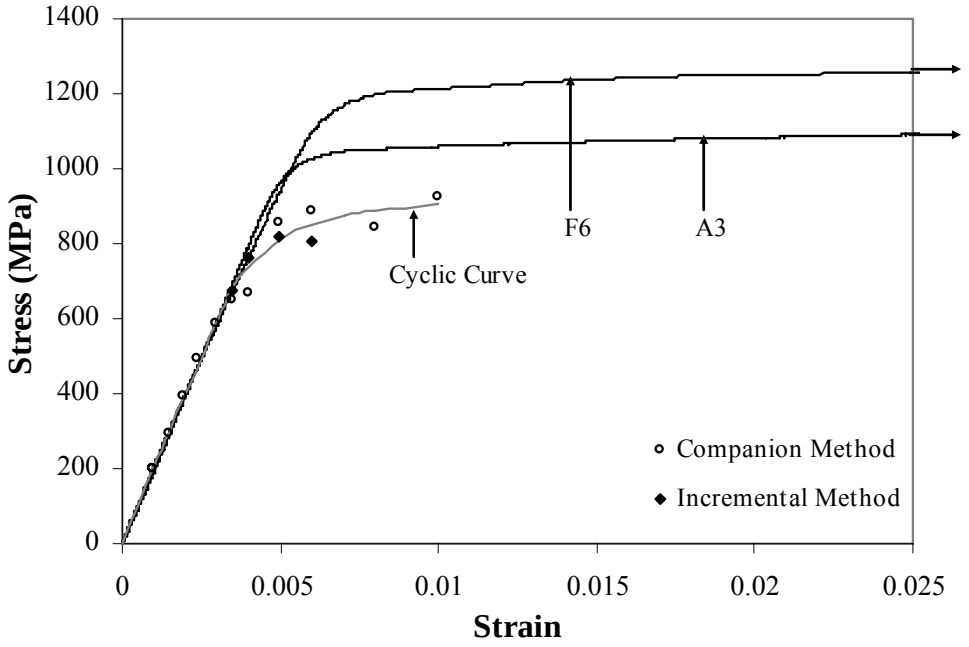

Figure 4.2 - Monotonic and Cyclic Stress-Strain Curves of Truncated Cone Specimens

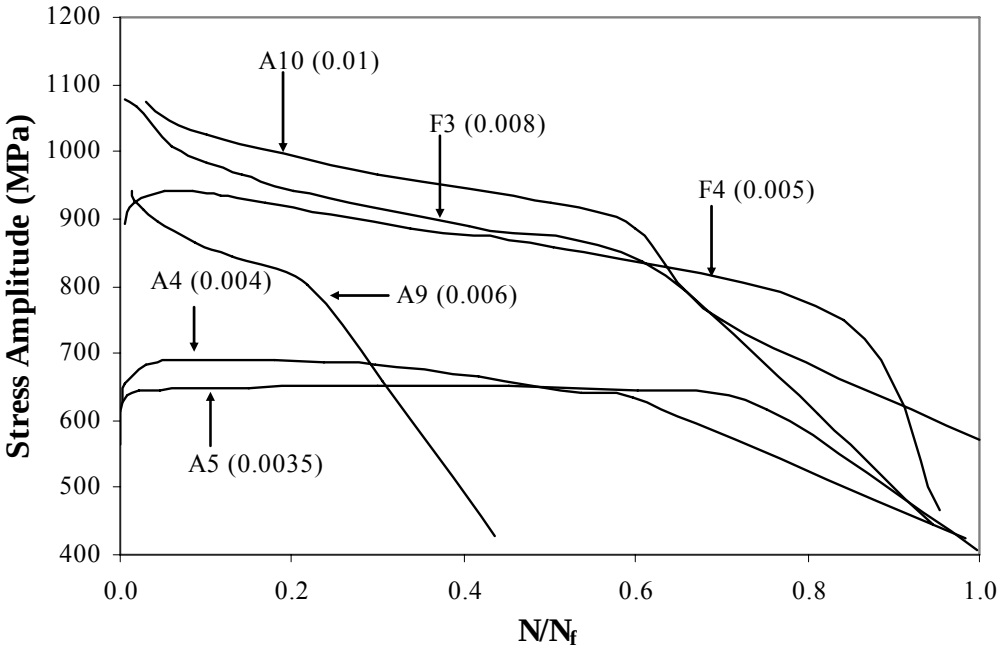

Figure 4.3 - Stress Amplitude vs. Normalized Applied Cycles for LCF Specimens

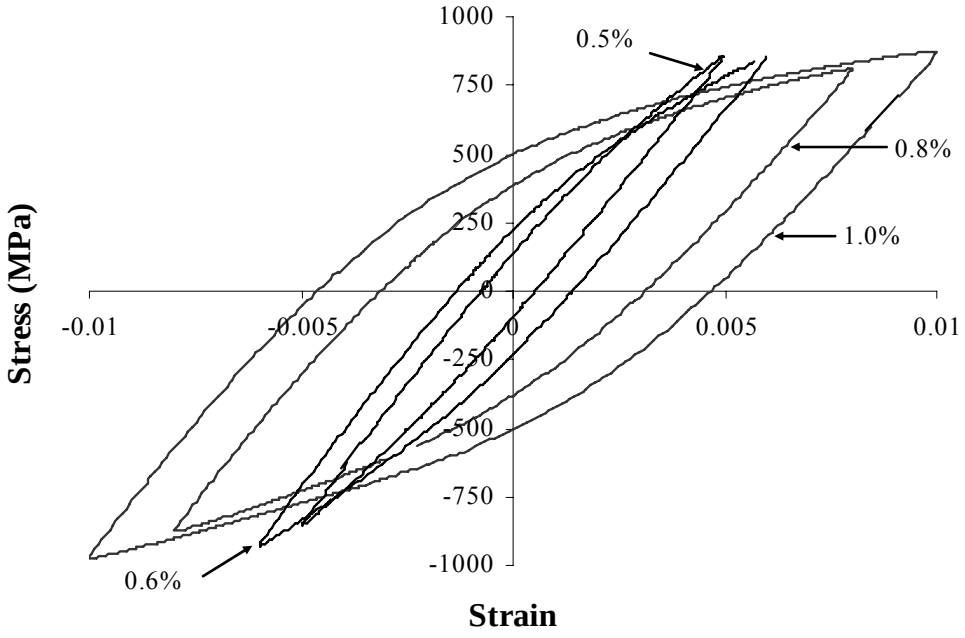

Figure 4.4 - Stress-Strain Hysteresis Loops for LCF Testing (Companion Method)

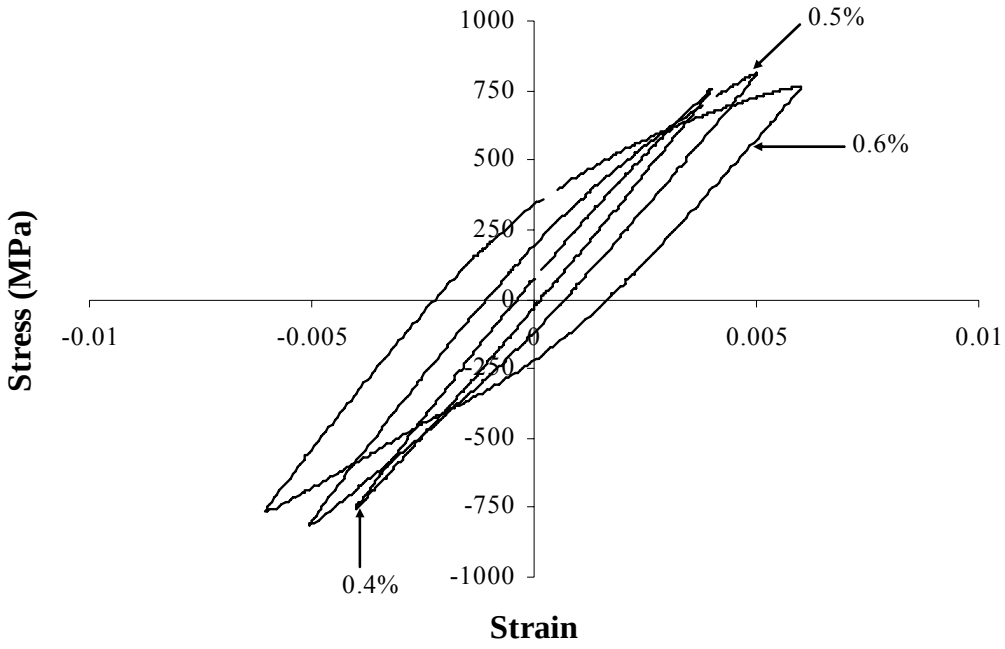

Figure 4.5 - Stress-Strain Hysteresis Loops for LCF Testing (Incremental Method)

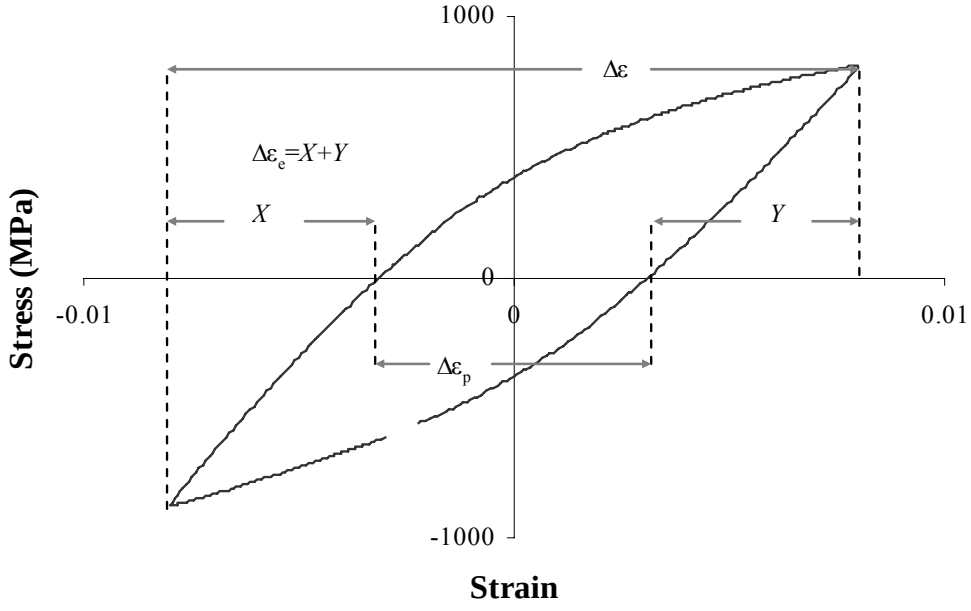

Figure 4.6 - Graphical Representation of Total, Elastic, and Plastic Strains

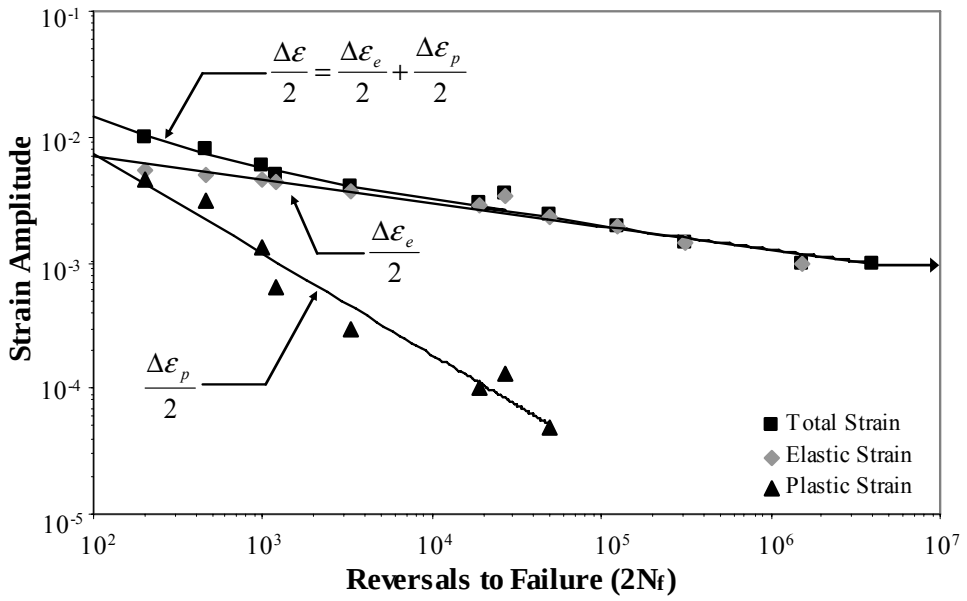

Figure 4.7 - Total, Elastic, and Plastic Strain-Life Data of Truncated Cone Specimens

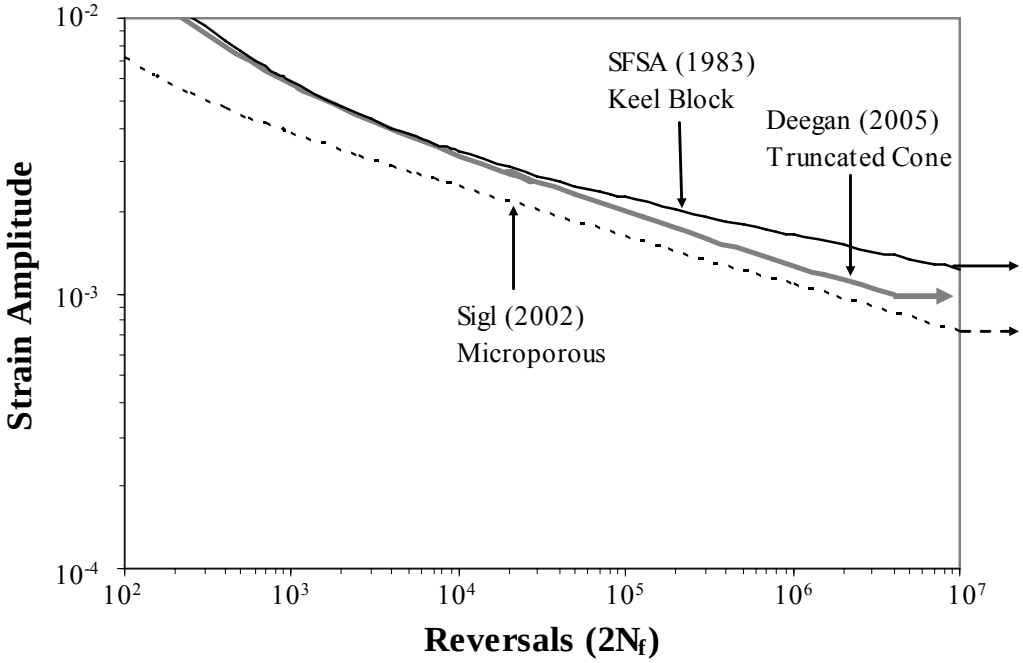

Figure 4.8 - Comparison of Strain-Life Curves

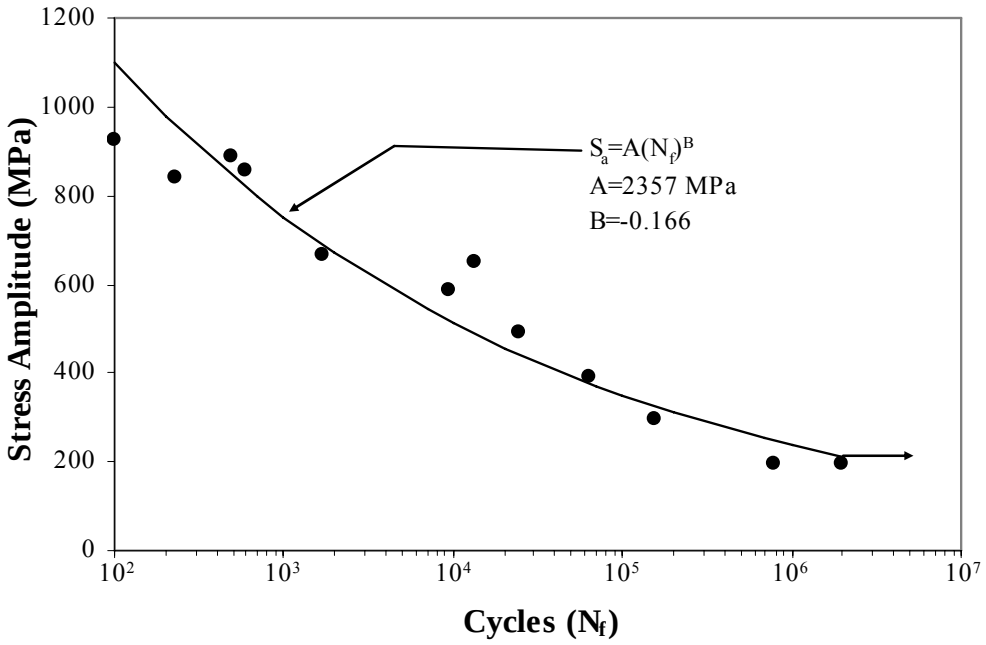

Figure 4.9 - Truncated Cone Specimen Stress-Life Data

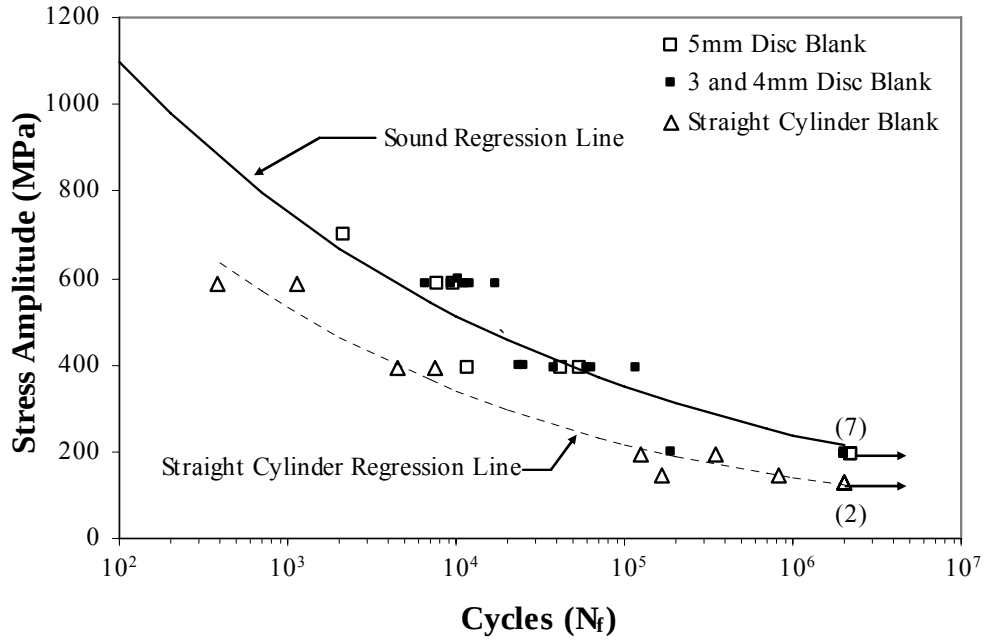

Figure 4.10 - Cylinder with Disc Specimen and Straight Cylinder Specimen Data Superimposed on Sound S-N Curve

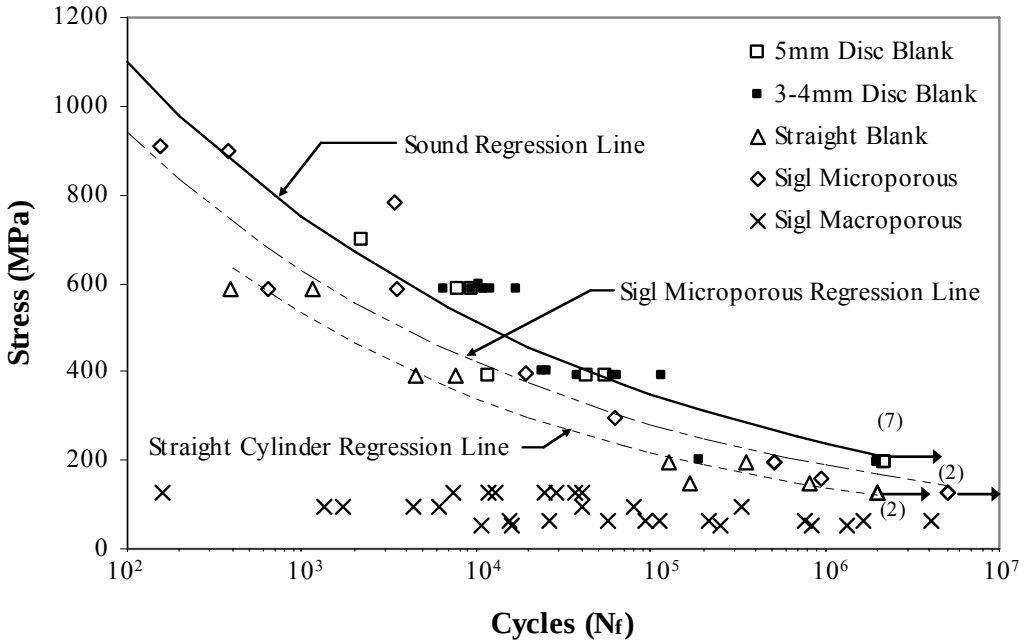

Figure 4.11 - Sigl's Results plotted with the Current Study's Results

CHAPTER 5: FRACTOGRAPHY

5.1 Fractography Procedure

After the specimens had been tested axially several of their fracture surfaces were examined, including both monotonic and fatigue specimens. As seen in Kyle Sigl's testing [2], there were two types of fatigue fracture; a monotonic type surface, and a more typical fatigue fracture surface. The monotonic type surface was jagged with little evidence of fatigue crack growth (FCG). This type of fracture happened in monotonic specimens as well as specimens that were tested at higher than 0.004 strain amplitude where fatigue lives were less than 1000 cycles. The other type, a typical fatigue fracture surface, was usually composed of two distinct regions. The first was a macroscopically flat region that showed fatigue facets microscopically, that was typical of a FCG region. Additionally at the edge of the specimen in this region a crack nucleation or crack initiation site was observed. The second region was the final fracture region that had a raised or lowered edge, also known as a shear lip that usually occurred at a 45 º angle. The angle is indicative of fracture along the plane of the greatest shear stress that is characteristic of a final ductile fracture region. The specimens with the most evidence of fatigue crack growth were found in the HCF specimens. This includes all specimens machined from cylinder with disc blanks, straight cylinder blanks, and six specimens from the truncated cone blanks. All specimen radiographs with indicated fracture zones are available from the University of Iowa Solidification Labaoratory upon request.

Using 8x and 16x magnifying glasses, all the specimen fracture surfaces were examined by eye to choose representative fractures from the three different casting geometries: specimens that were machined from truncated cones, specimens machined from cylinders with discs, and specimens machined from straight cylinder blanks. In addition to geometry, the stress/strain amplitudes of the specimens also served as criteria for choosing specimens to further examine. Four specimen fracture surfaces were chosen

from the truncated cones, each at different stress/strain amplitude levels. The different levels included were a monotonic specimen, a specimen tested at an amplitude of 0.004 in strain control, and two specimens tested in stress control at amplitudes of 588 MPa and 392 MPa. The latter two specimens corresponded to stress levels in the other geometry specimens. For the cylinder w/ disc blank specimens, three specimens were chosen; one from a stress level of 588 MPa, and two from the 392 MPa stress level. These two stress amplitudes had caused fatigue fracture in the cylinder with disc specimens. Four specimen surfaces were examined from the straight cylinder blank geometry. Two specimens with stress amplitudes of 588 MPa and 392 MPa which were the same stress amplitude as the other casting geometries, and two at the lower stress amplitudes that caused fracture; 196 and 147 MPa.

A Hitachi S-4000 scanning electron microscope (SEM) located at The University of Iowa Central Microscopy Facilities was employed to conduct fractography. In order to view the specimen fracture surfaces in the SEM, the sections containing the fracture surfaces were cut from the rest of the specimen. Using a precision band saw at the Furman Machine Shop, the fracture surfaces were cut from the specimen, so they would fit into the vacuum chamber of the SEM. The 1-2 cm tall sections were mounted onto an aluminum stage using non-reactive colloidal silver liquid cement. The specimens were washed in acetone to remove any contaminants that could affect the image. Images were taken between 20x and 1500x inline with the applied axial load. At the lowest magnification of 20x, the entire surface could not be fit into the viewing screen, so a composite of four images was constructed. This composite served as a macroscopic image to examine the surface and a reference for higher magnification images.

5.2 Truncated Cone Blank Specimens

Figure 5.1 shows a macroscopic view of a monotonic fracture surface. This image is also similar to higher amplitude cyclic specimens such as 0.01, 0.008, 0.006, and 0.005

strain amplitudes tested on the truncated cone specimens. The surface tends to be very uneven and shows no definitive evidence of crack nucleation. On this particular specimen the entire surface is slanted at 45º with no flat regions. The high amplitude cyclic specimens also had no flat surfaces and were jagged and uneven. Figure 5.2 shows an image of what the majority of the specimen surfaces looked like at a magnification of 1500x. This image is an example of ductile dimpling, which is characteristic of a high energy fracture with significant local ductile deformation. This is consistent with the monotonic tests that showed necking before fracture. Another feature on the fracture surface is shown in Figure 5.3. This image was taken at 45x and shows evidence of porosity or dendrite development. Dendrites can be the result of the liquid metal crystallizing as a free surface. The presence of dendrites often indicates porosity. The solidification model for the truncated cone predicted less than 1% porosity; however from the image it was not possible to quantitatively determine the size of the pore from the fracture surface. A non-uniform surface makes it difficult to determine a ratio of pore diameter to cross sectional area; nonetheless there is evidence of microporosity in all the truncated cone blank specimens examined for fractography.

Figure 5.4 shows the fatigue surface at 20x of a specimen conducted in strain control at a cyclic strain amplitude of 0.004 that lasted just over 1000 cycles. Unlike Figure 5.1, this surface has two distinct macroscopic regions that are separated by an artificial white line in Figure 5.5. The darker region represents the FCG region, while the lighter colored area was the region for final fracture. Figures 5.6 and 5.7 are characteristic images of these regions at 1500x respectively. The fatigue crack growth region has fatigue facets which cover the area where the crack had propagated before the specimen fractured. During each cycle the crack opens and closes and creates the surface shown in Figure 5.6. Figure 5.7 shows the final fracture region which is similar to that of the monotonic specimen. Ductile dimpling is evident, and the macroscopic surfaces are angled at 45º and more uneven than the FCG region. This fracture surface also showed

similar evidence of porosity and dendrite formation that was seen in the monotonic specimen. The occurrence of this is especially interesting at the top left of Figure 5.4 which is shown magnified in Figure 5.8. This image of the area that shows the possible crack nucleation site at 50x where there is dendritic formation at the outer edge of the specimen. This likely contributed to the formation of a crack.

Specimens tested at a constant cyclic stress amplitude exhibited similar characteristics to the constant cyclic strain amplitude test specimen, $\varepsilon_a = 0.004$, that was shown in Figure 5.4. Figure 5.9 shows the fracture surface of a truncated cone specimen that lasted ~10 000 cycles at a S_a of 588 MPa. Two separate regions are visible and are artificially separated by a white line in Figure 5.10. Again, the darker region showed evidence of fatigue facets that are characteristic of FCG, while the lighter region had ductile dimpling and sharper angles. Figure 5.11 shows a 20x image fracture surface of a truncated cone specimen that had a life of ~60 000 cycles at a S_a of 392 MPa. The left side of the image contains an elevated shear lip that under a magnification of 1500x reveals ductile dimpling, shown in Figure 5.12. By examining the right side of the 20x image there is an indication that this is where the crack nucleated. Figure 5.13 shows a magnified image of this area with evidence of porosity near the surface of the specimen, which again is the likely cause of crack nucleation.

5.3 Cylinder with Disc Blank Specimens

The cylinder with disc blank specimens were tested under HCF using stress control, therefore they were expected to have longer fatigue lives. There should be evidence of the two fracture surface regions described previously: the FCG region and the final fracture region. The first specimen tested at a S_a of 599 MPa is shown at a magnification of 20x in Figure 5.14 and had a fatigue life of ~10 000 cycles. Figure 5.15 shows the same specimen with a line differentiating the two regions. In this case the darker top region is the shear lip and the final fracture region. An image at 1500x, Figure

5.16, shows evidence of ductile dimpling at the shear lip region. The lighter FCG region indicates fatigue facets at the same magnification and is shown in Figure 5.17.

The examined cylinder w/ blank specimens show evidence of both types of fracture surface regions, but tend to have a more textured surface than the truncated cone specimens. This is due to the increased porosity which affects the axial direction of the crack as it proceeds across the cross section. As the crack encounters a pore, the pore shape is incorporated into the crack which can alter the path of the crack. Another specimen tested at a stress amplitude of 392 MPa is shown in Figure 5.18 and shows features such as pores in the path of the fatigue crack. The fatigue crack initiates at the far left, and propagates toward the shear lip on the far right, but at the center an uneven feature is evident. A pore is shown at higher magnification in Figure 5.19 and has indications of dendrite formation on a scale greater than seen in the truncated cone blank specimens. This is consistent with the radiographs and the porosity models that predict a higher amount of macroporosity. Figure 5.20 shows porosity near the outer edge of the specimen and likely contributed to initiation of the fatigue crack. Another specimen tested at a S_a of 392 MPa is shown at a magnification of 20x in Figure 5.21. This particular specimen has two FCG regions, one from the left and one from the right. These regions are indicated by white lines in Figure 5.22 along with two major pores that are boxed. The pore in the center is shown in Figure 5.23 and is at the edge of the two fatigue regions. The lower pore is shown in Figure 5.24, and although it is entirely in the final fracture region it may have altered the path of the fatigue crack. In both of these figures there is substantial dendrite development.

5.4 Straight Cylinder Blank Specimens

The straight cylinder specimens were tested using HCF at the three stress levels of the cylinder with disc blank specimens, but because run-out was not achieved two lower stress levels were also tested. The specimens tested at 588 and 392 MPa each lasted

~1 000 and ~8 000 cycles, and are shown in Figures 5.25 and 5.26 respectively. Macroscopically it was difficult to distinguish the two types of fracture surfaces from each other because of the uneven texture. This is characteristic of the high cyclic strain amplitude fractures seen in the truncated cone specimens. By analyzing the surface at higher magnifications, it was evident that there was a FCG region, as shown in Figure 5.27. A final fracture region with ductile dimpling is shown in Figure 5.28. The specimen tested at 392 MPa is shown in Figure 5.29, and contained features that looked like large fatigue facets, and indicates a higher rate of crack propagation. An uneven surface was observed in cylinder with disc specimens and this was an indication of greater porosity. At a magnification of 100x the surface of the specimen tested at 588 MPa has dendrite formation as shown in Figure 5.30. This occurs over much of the surface and indicates a greater amount of porosity. The specimen tested at 392 MPa had a center pore shown in Figure 5.31. At 100x magnification this figure shows extensive dendrite formation.

The specimens tested at lower stress levels of 196 and 147 MPa showed signs of porosity, but the separate fatigue regions were more defined as seen macroscopically in Figures 5.32 and 5.33. The lighter region at the bottom of the 196 MPa specimen is the shear lip and at a magnification of 1500x ductile dimpling is evident as shown in Figure 5.34. The darker regions in the upper half of the surface show evidence of FCG found in Figure 5.35. This specimen also had significant centerline porosity with extensive dendrite formation shown in Figure 5.36 at 100x. The specimen tested at 147 MPa contained common fatigue features where the shear lip located at the upper left of Figure 5.33 contained ductile dimpling as was seen at higher magnification. Likewise the FCG region along the majority of the lower right half of the fracture surface showed fatigue facets when viewed at higher magnification. This specimen does not show as much porosity as the previous specimen, but deep dendrite formation is still observed in Figure 5.37. Figure 5.38 shows the lower right of the same specimen where porosity probably initiated the fatigue crack.

5.5 Summary of Fractography Results

The truncated cone specimens exhibited two types of fatigue fracture. The first type of fracture looked similar to a monotonic fracture with mostly ductile deformation and little evidence of FCG. These fractures were seen in low fatigue life, high strain amplitude LCF specimens. The other type of fracture was a typical fatigue fracture. The typical fatigue fracture contained two regions, a FCG region, and a final fracture region. The FCG region was generally flat and under higher magnifications showed fatigue facets. The final fracture region was usually angled at 45º and contained microscopic ductile dimples. Ductile dimples are a sign of a high energy ductile fracture. On the fracture surfaces of all the truncated cone specimens examined there was evidence of dendrite formation. Dendrites can be an indicator of porosity, which was not expected to be seen in the truncated cone specimens. Additionally it was shown that the fatigue crack initiated at points of porosity near the surface on fatigue specimens. Although there is evidence of porosity, the size and amount cannot be determined from the raw fracture surface. Further analysis is undertaken using microscopy.

All the cylinder with disc specimens were tested in load control at low stress amplitudes, and all fractured at lives greater than 2 000 cycles. Because of this all the specimens examined showed typical fatigue fractures, with two fracture regions. When the regions are viewed under magnification they exhibit the same characteristics seen in the truncated cone specimens, i.e. with ductile dimpling in the final fracture region, and fatigue facets in the FCG region. The fracture surfaces were more uneven due to a greater amount of porosity found. Similar to the truncated cones, in the FCG region evidence of dendrites were present at the crack initiation sites.

The straight cylinder specimens showed the two types of fracture seen in the truncated cone specimens. The ductile fracture specimens had fatigue lives of less than 10 000 cycles, while specimens that had more than 10 000 cycles had typical fatigue fractures. Under magnification areas of ductile dimpling were found indicating ductile

fracture in both types of fracture. Areas with larger fatigue facets were also found indicating FCG in the shorter life specimens. For the longer life specimens they showed the same characteristics previously described with the other casting geometries. The fracture surfaces contained extensive dendrite formation and hence more developed porosity when compared to the other casting geometries. The pores in these specimens also had more texture and extended into the specimen more than what was seen in the cylinder with disc specimens.

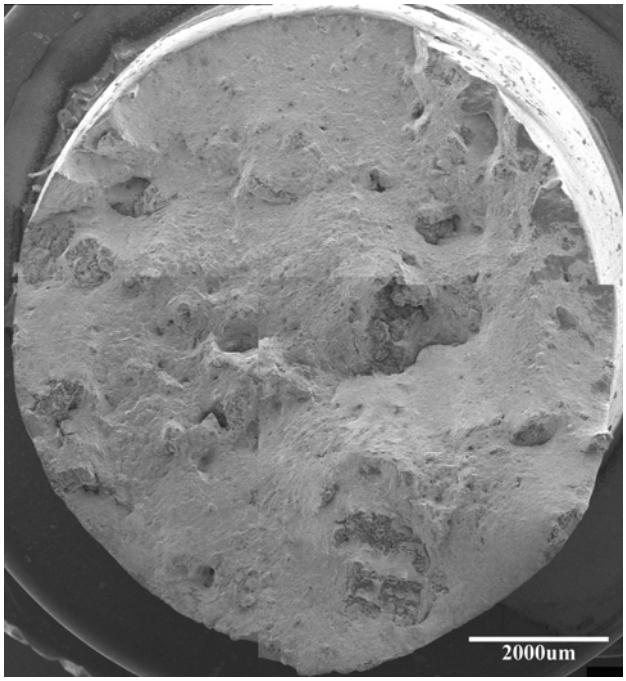

Figure 5.1 - Macroscopic View of a Sound Monotonic Test Specimen Fracture Surface (Specimen A3)

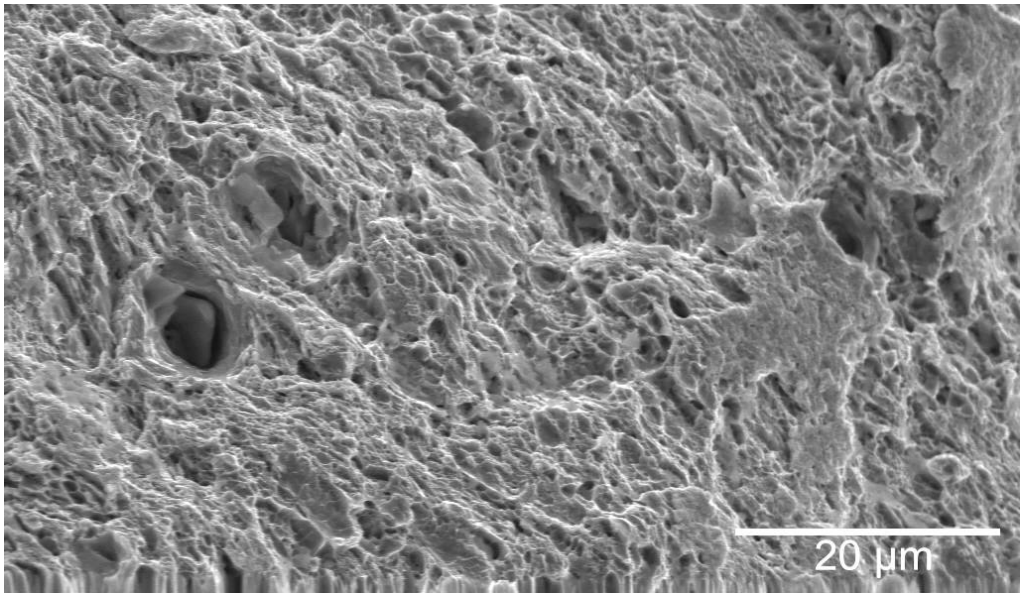

Figure 5.2 - Microscopic View of a Sound Monotonic Test Specimen Fracture Surface (Specimen A3)

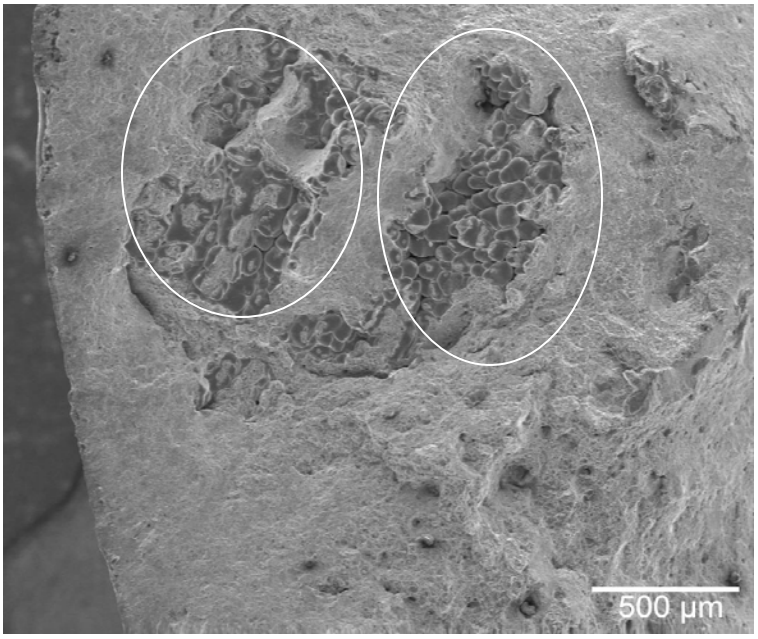

Figure 5.3 - Dendrite Development on a Sound Monotonic Test Specimen Fracture Surface (Specimen A3)

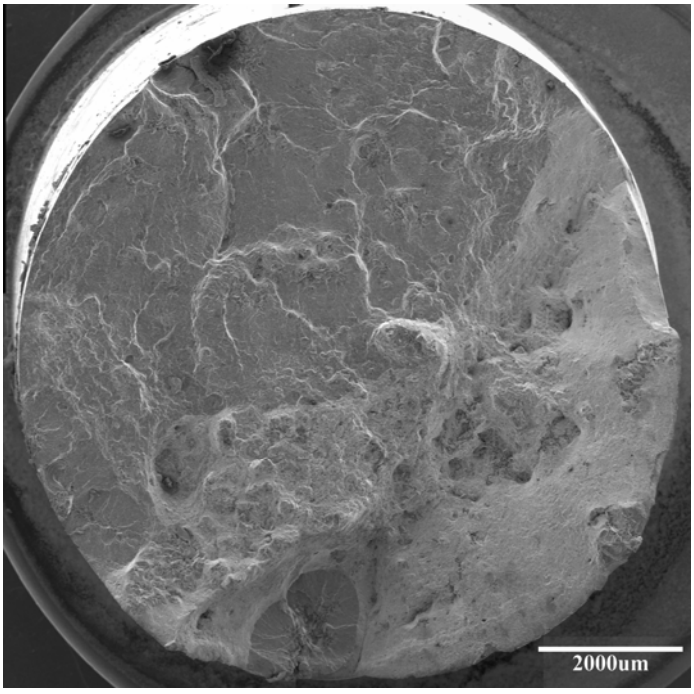

Figure 5.4 - Macroscopic View of a Strain Control Truncated Cone Specimen Fracture Surface, $\varepsilon_a = 0.004$ (Specimen A4)

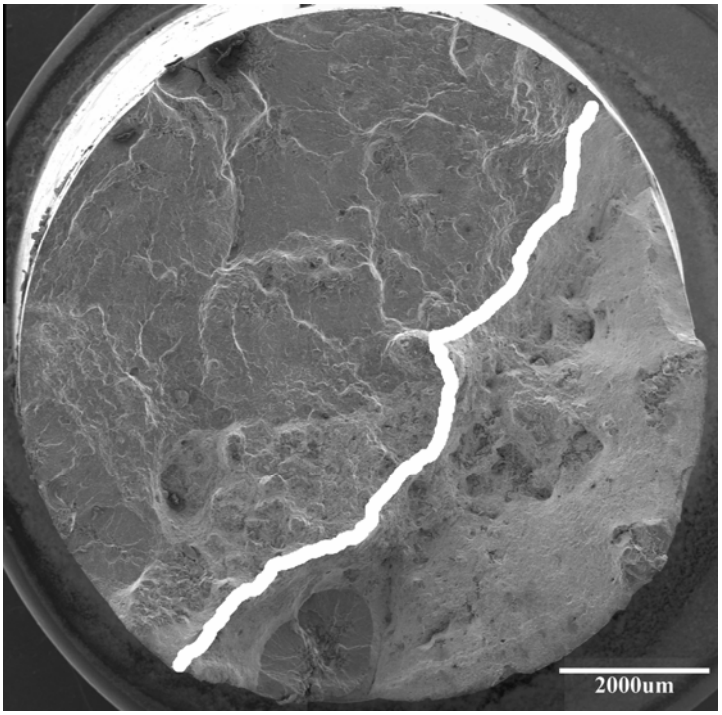

Figure 5.5 - Fracture Regions Divided by an Inserted Line on a Strain Control Truncated Cone Specimen, $\varepsilon_a = 0.004$ (Specimen A4)

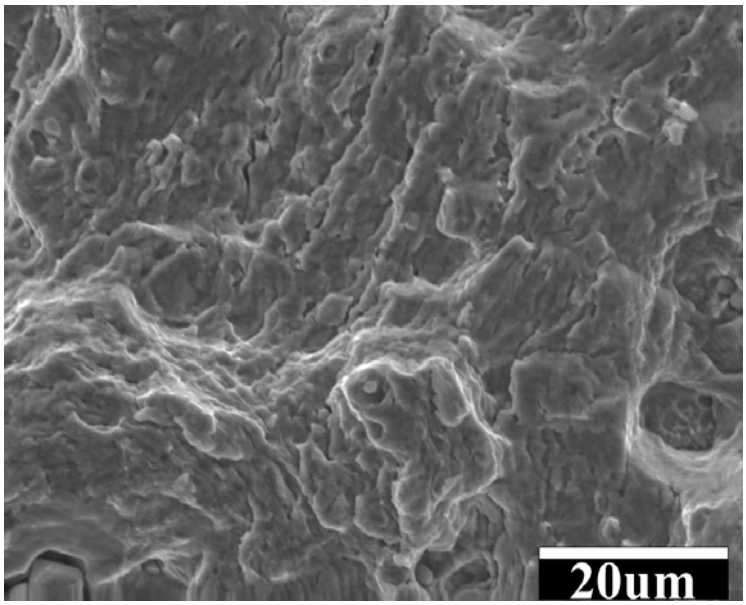

Figure 5.6 - View of the FCG Region on a Strain Control Truncated Cone Specimen Fracture Surface, $\varepsilon_a = 0.004$ (Specimen A4)

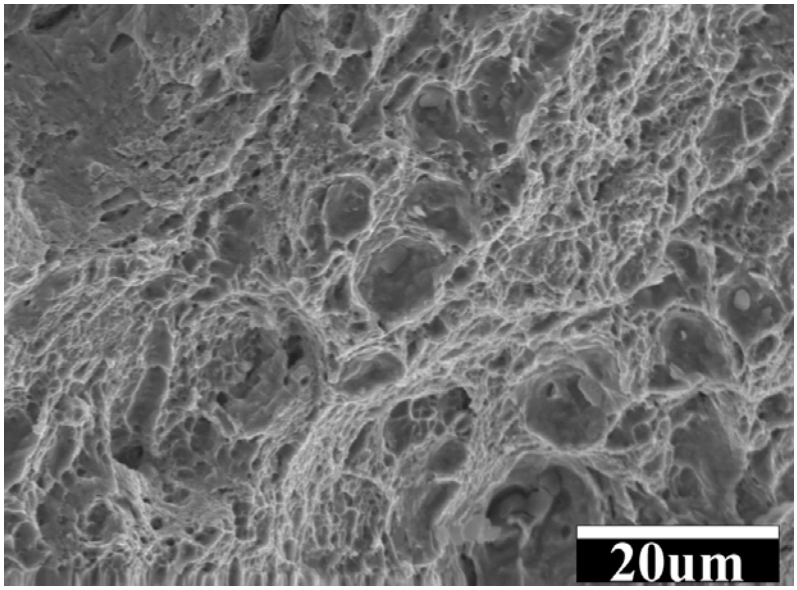

Figure 5.7 - Microscopic View of the Final Fracture Region on a Strain Control Truncated Cone Specimen Fracture Surface, $\varepsilon_a = 0.004$ (Specimen A4)

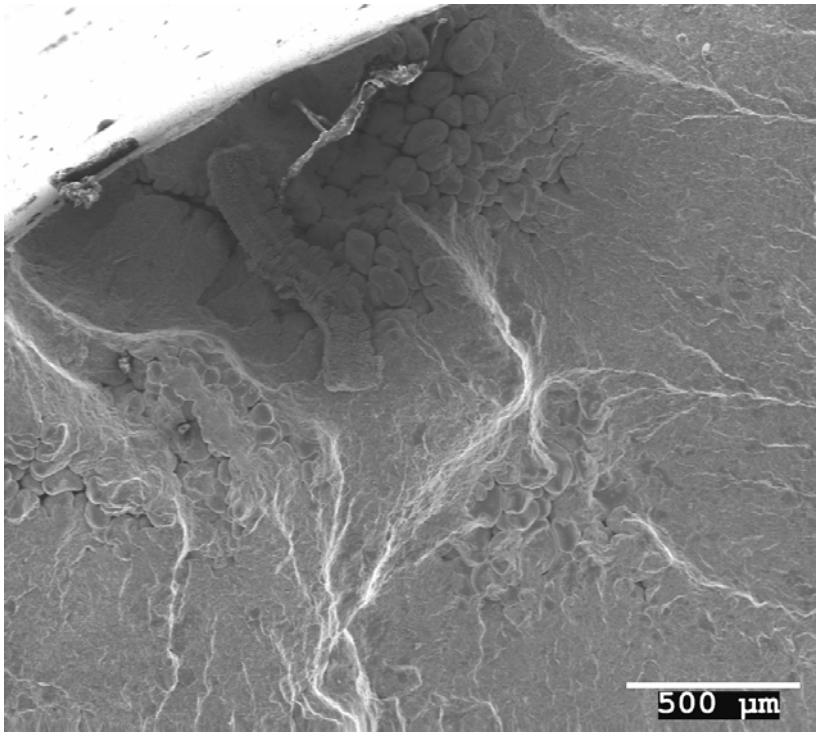

Figure 5.8 - View of the Crack Nucleation Site of a Strain Control Truncated Cone Specimen Fracture Surface, $\varepsilon_a = 0.004$ (Specimen A4)

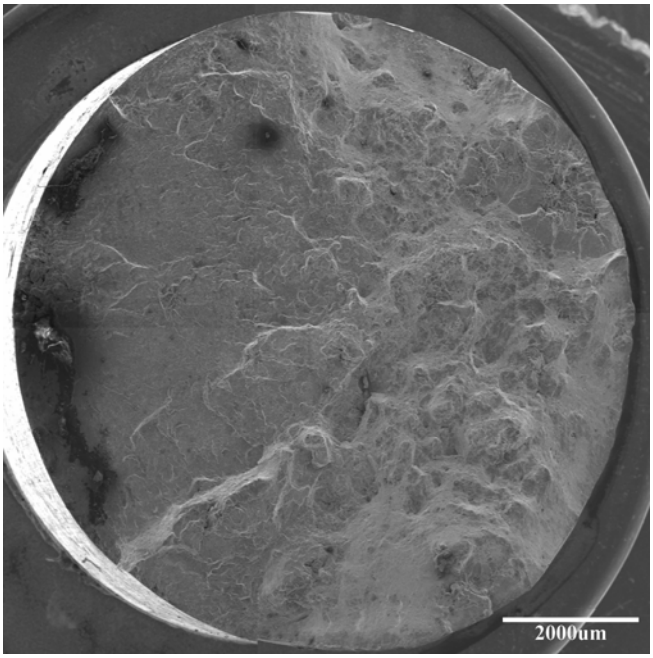

Figure 5.9 - Macroscopic View of a Truncated Cone Specimen Fracture Surface, S_a = 587 MPa (Specimen A6)

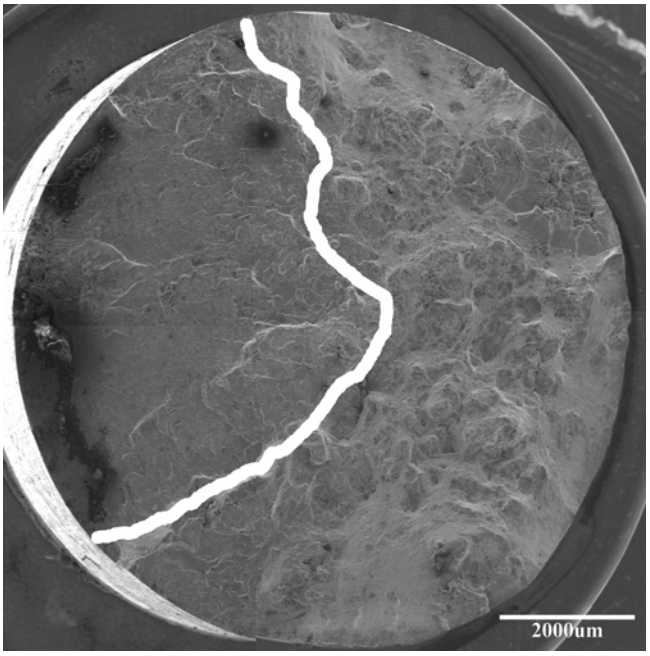

Figure 5.10 - Fracture Regions Divided by an Inserted Line on a Stress Control Truncated Cone Specimen, S_a = 587 MPa (Specimen A6)

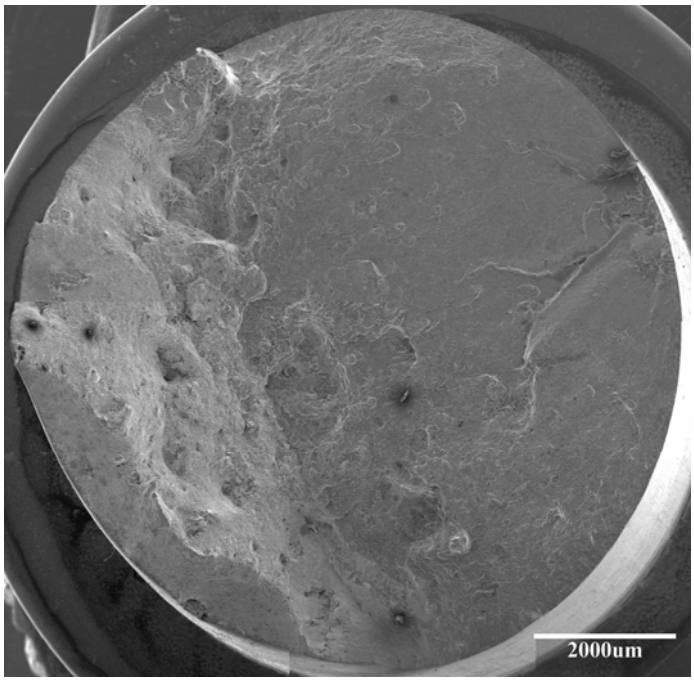

Figure 5.11 - Macroscopic View of a Truncated Cone Specimen Fracture Surface, S_a = 394 MPa (Specimen F8)

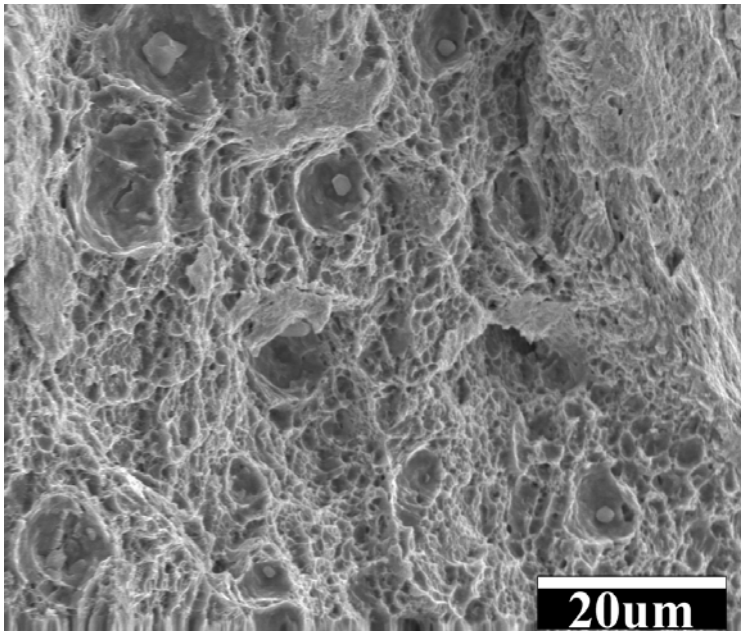

Figure 5.12 - Microscopic View of the Final Fracture Region on a Stress Control Truncated Cone Specimen Fracture Surface, S_a = 394 MPa (Specimen F8)

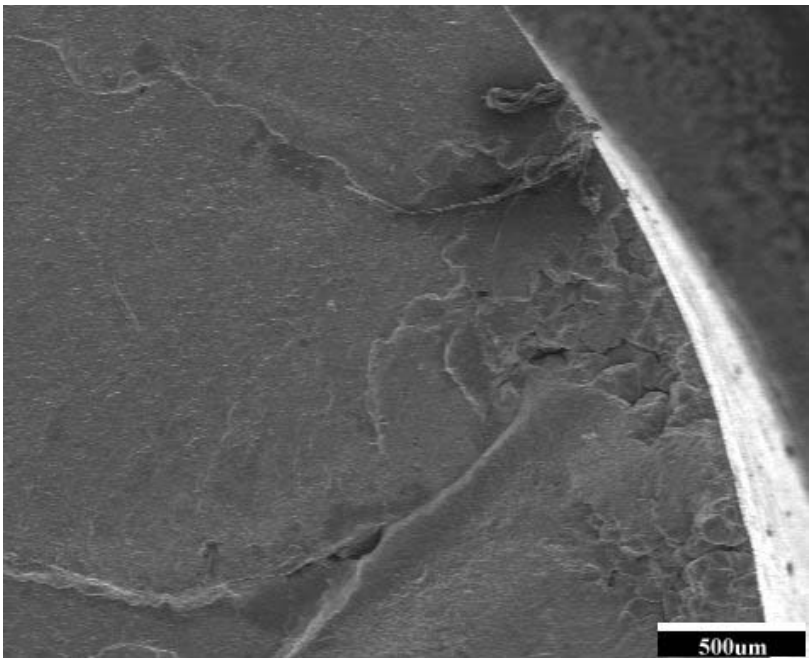

Figure 5.13 - View of the Crack Nucleation Site of a Stress Control Truncated Cone Specimen Fracture Surface, S_a = 394 MPa (Specimen F8)

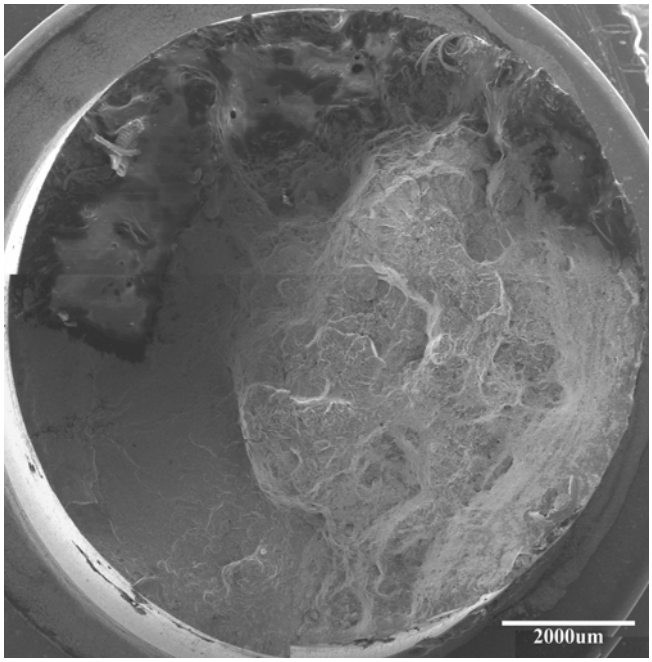

Figure 5.14 - Macroscopic View of a Cylinder with Disc Specimen Fracture Surface, S_a = 588 MPa (Specimen E7)

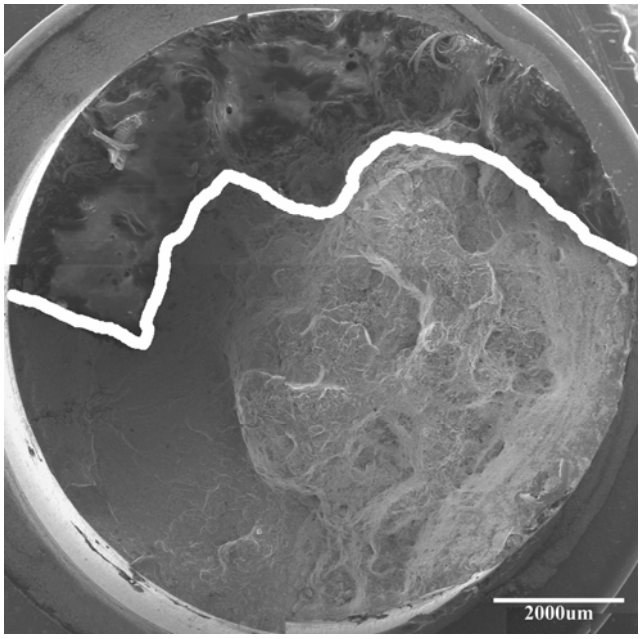

Figure 5.15 - Fracture Regions Divided by an Inserted Line on a Stress Control Cylinder with Disc Specimen, S_a = 588 MPa (Specimen E7)

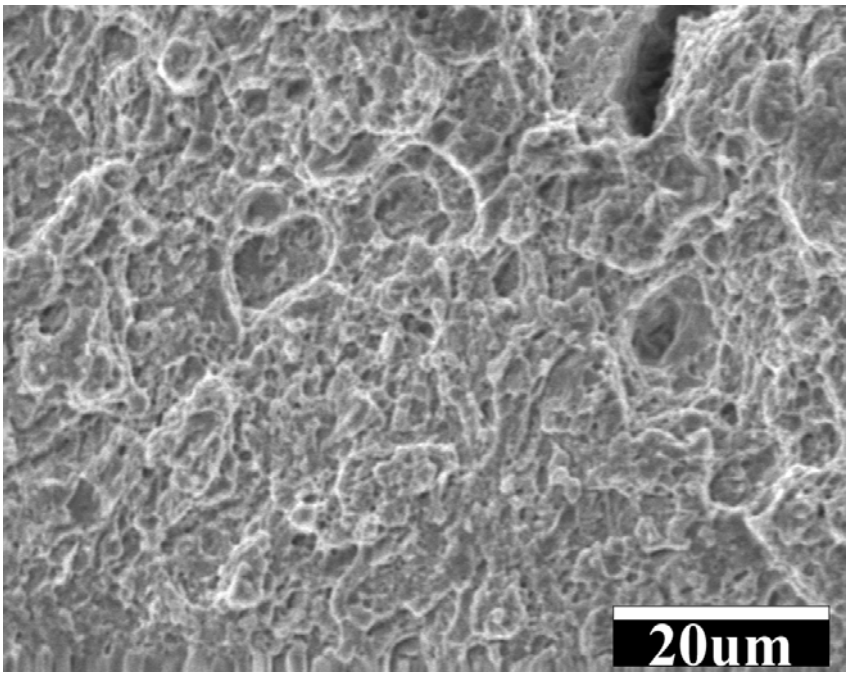

Figure 5.16 - Microscopic View of the Final Fracture Region on a Cylinder with Disc Specimen Fracture Surface, S_a = 588 MPa (Specimen E7)

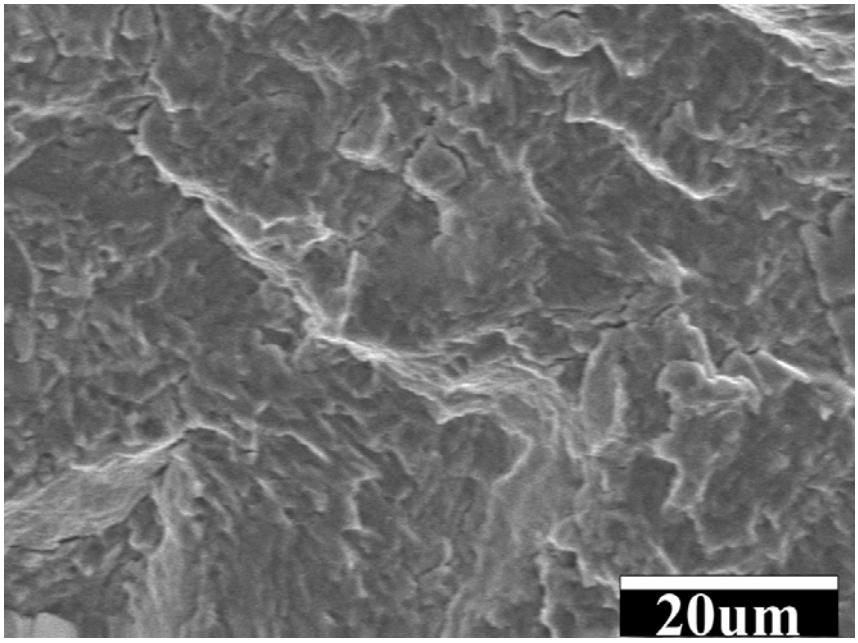

Figure 5.17 - Microscopic View of the FCG Region on a Cylinder with Disc Specimen Fracture Surface, S_a = 588 MPa (Specimen E7)

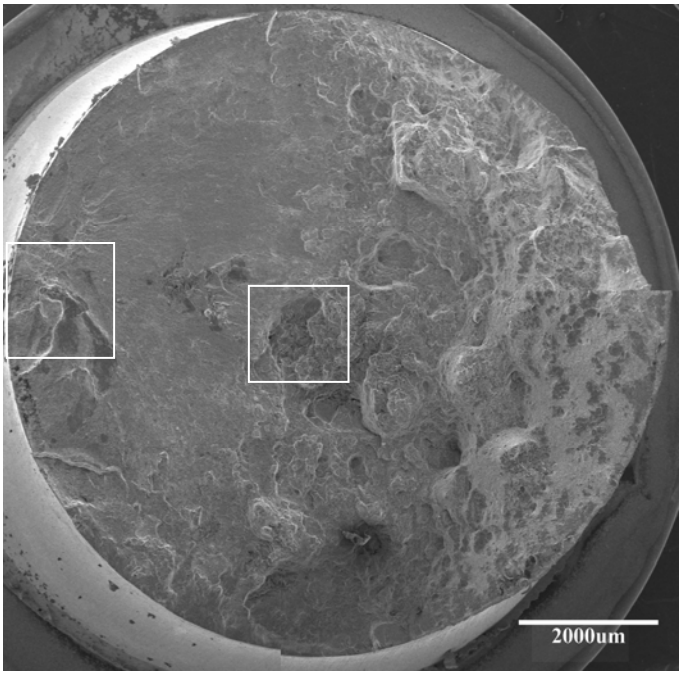

Figure 5.18 - Macroscopic View of a Cylinder with Disc Specimen Fracture Surface, S_a = 392 MPa (Specimen E5)

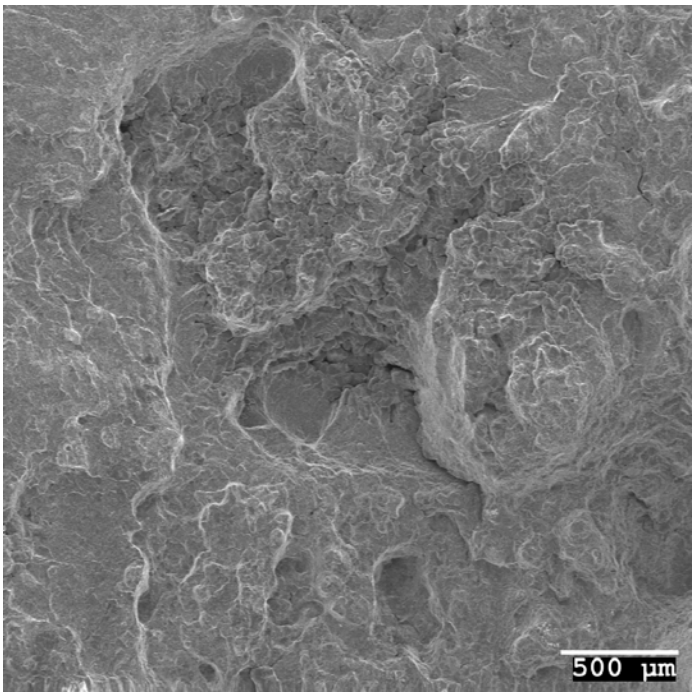

Figure 5.19 - View of a Center Pore on Cylinder with Disc Specimen Fracture Surface, S_a = 392 MPa (Specimen E5)

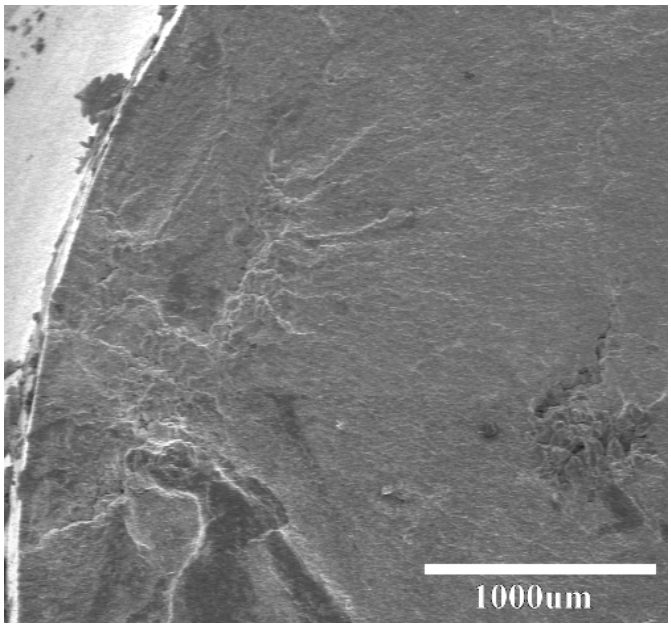

Figure 5.20 - View of the Crack Initiation Site of a Cylinder with Disc Specimen Fracture Surface, S_a = 392 MPa (Specimen E5)

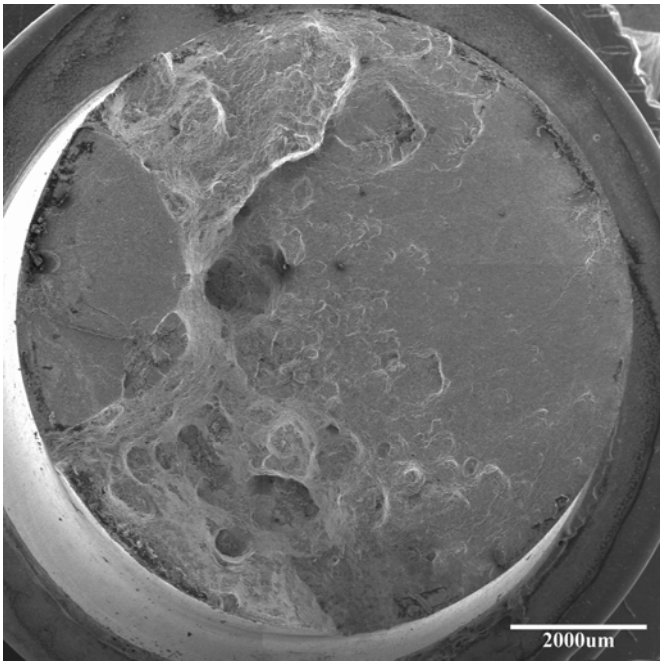

Figure 5.21 - Macroscopic View of a Cylinder with Disc Specimen Fracture Surface, S_a=392 MPa (Specimen H5)

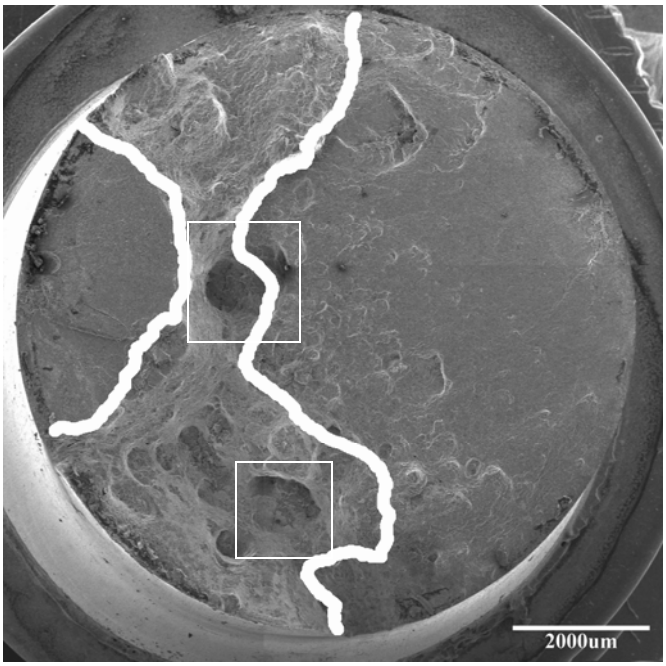

Figure 5.22 - Fracture Regions Divided by Inserted Lines and Two Major Pores Boxed on a Cylinder with Disc Specimen, S_a=392 MPa (Specimen H5)

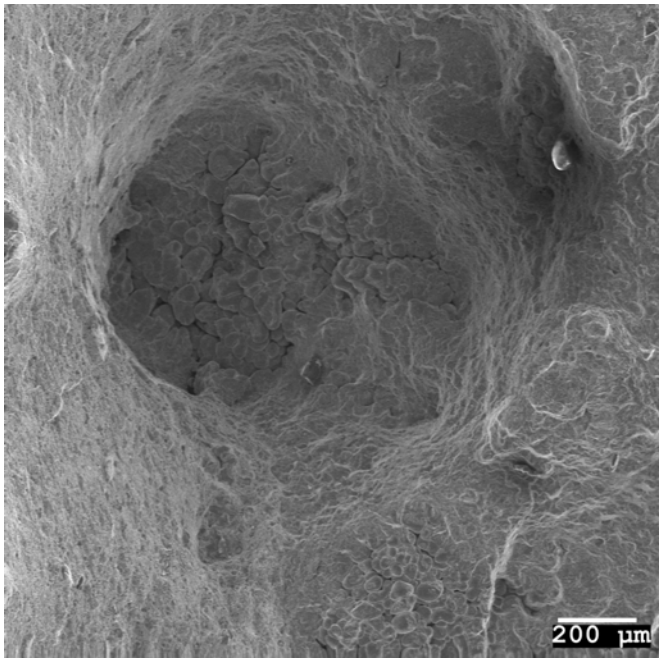

Figure 5.23 - Center Pore on a Stress Control Cylinder with Disc Specimen, S_a = 392 MPa (Specimen H5)

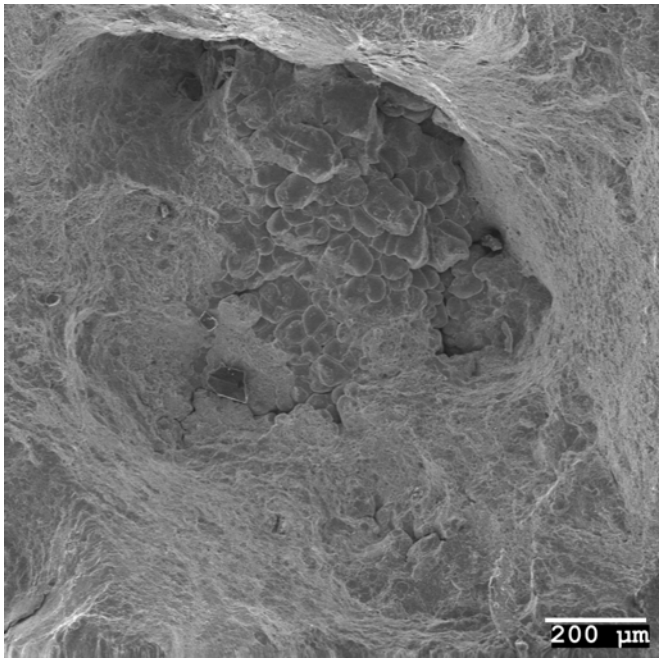

Figure 5.24 - Lower Pore on a Stress Control Cylinder with Disc Specimen, S_a = 392 MPa (Specimen H5)

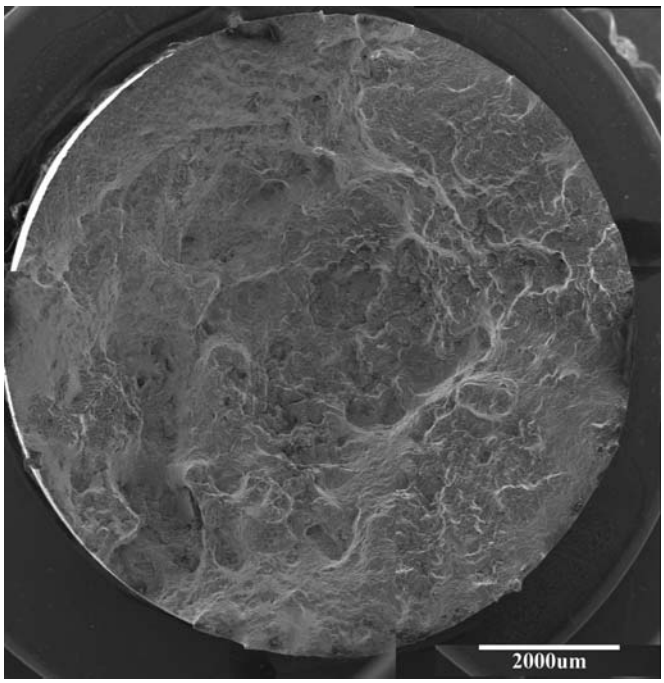

Figure 5.25 - Macroscopic View of a Straight Cylinder Specimen Fracture Surface, S_a = 588 MPa (Specimen G5)

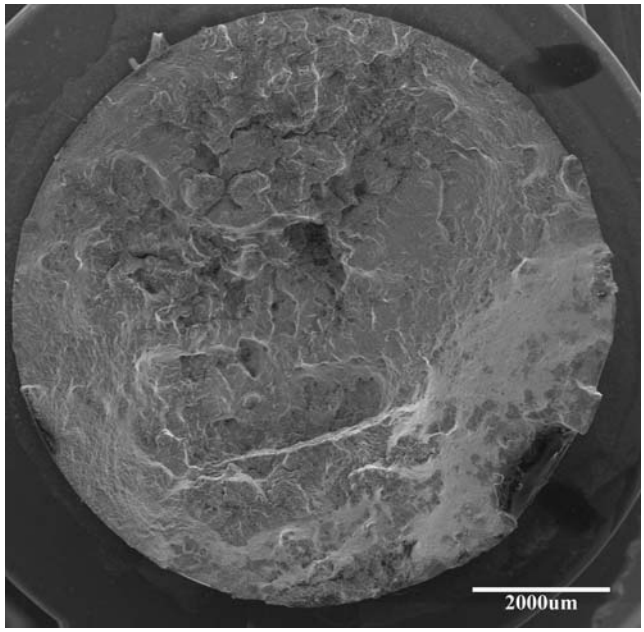

Figure 5.26 - Macroscopic View of a Straight Cylinder Specimen Fracture Surface, S_a = 392 MPa (Specimen G7)

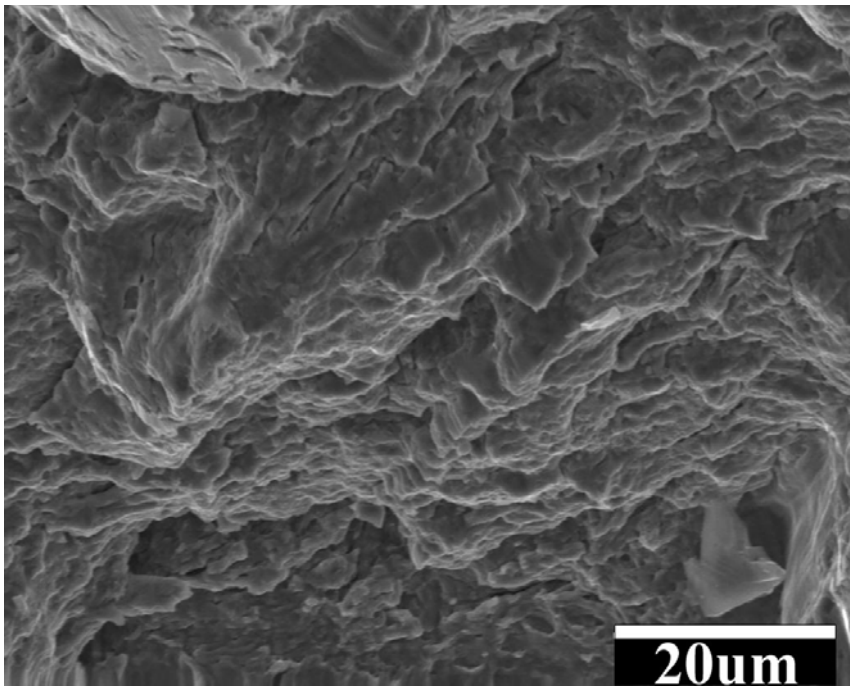

Figure 5.27 - Microscopic View of the FCG Region on a Straight Cylinder Specimen Fracture Surface, S_a = 588 MPa (Specimen G5)

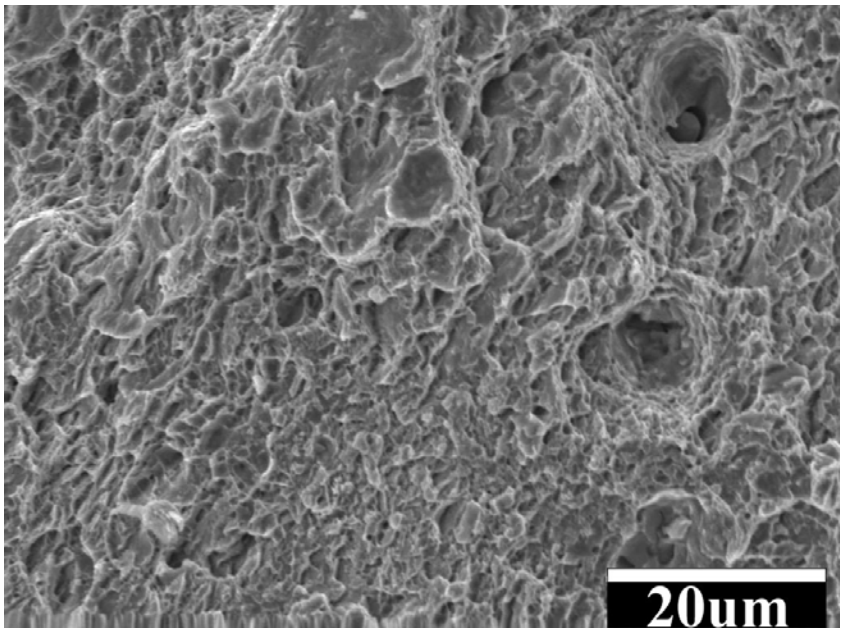

Figure 5.28 - Microscopic View of the Final Fracture Region on a Straight Cylinder Specimen Fracture Surface, S_a = 588 MPa (Specimen G5)

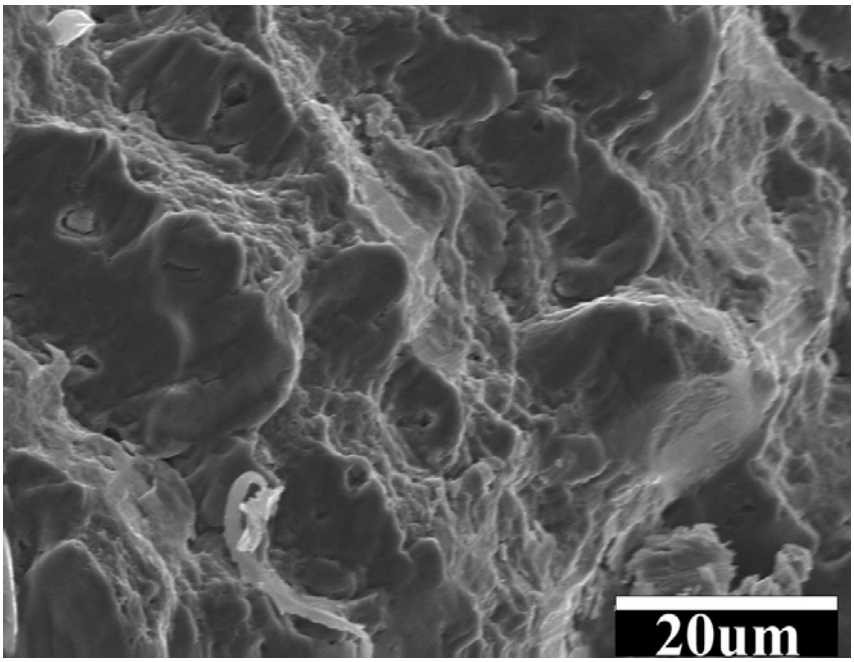

Figure 5.29 - Microscopic View of Large Fatigue Facets of the FCG Region on a Straight Cylinder Specimen Fracture Surface, S_a = 392 MPa (Specimen G7)

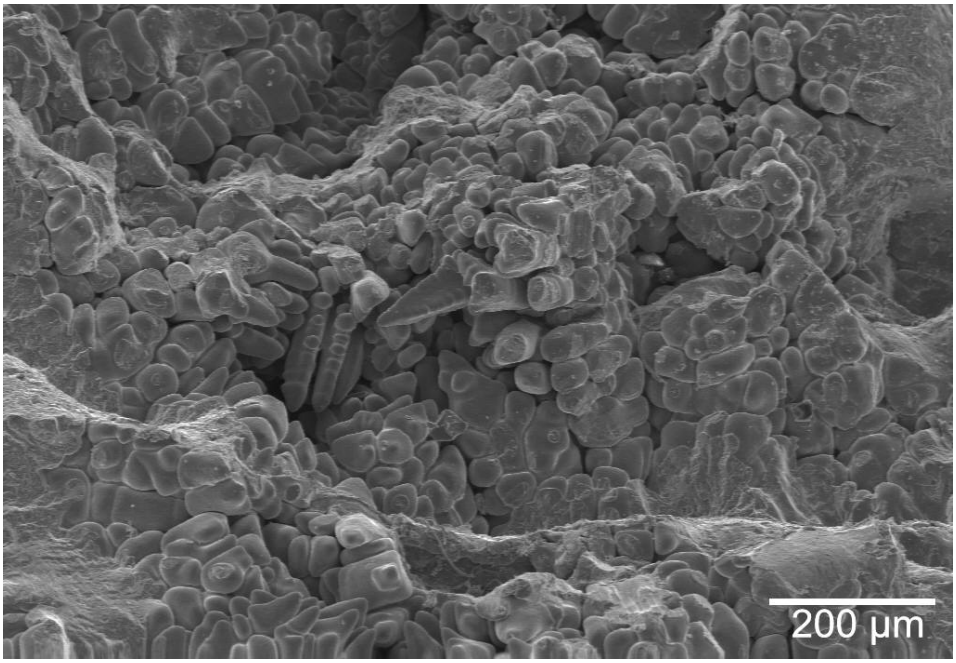

Figure 5.30 - Dendrite Formation on Straight Cylinder Specimen Fracture Surface, S_a = 588 MPa (Specimen G5)

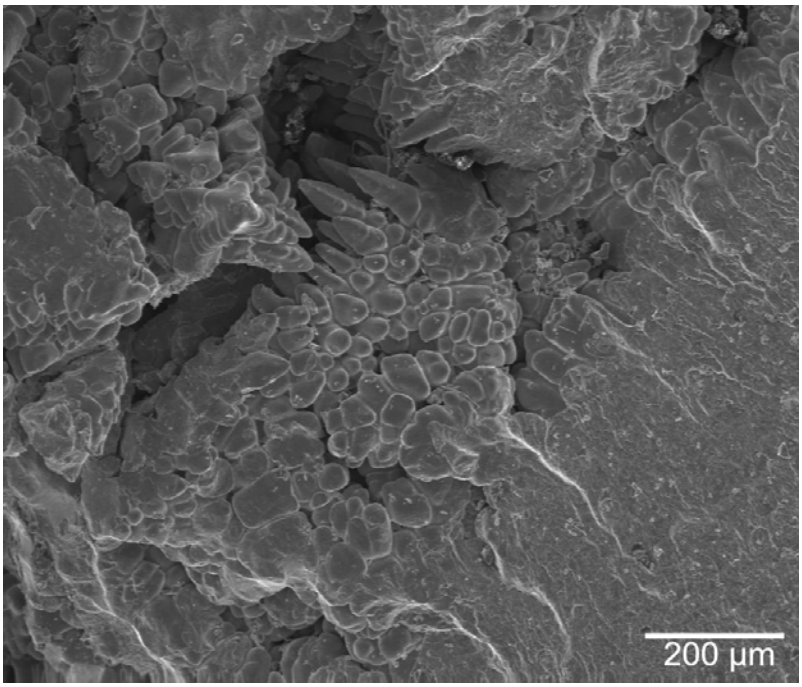

Figure 5.31 - Extensive Dendrite Formation on Straight Cylinder Specimen Fracture Surface, S_a = 392 MPa (Specimen G7)

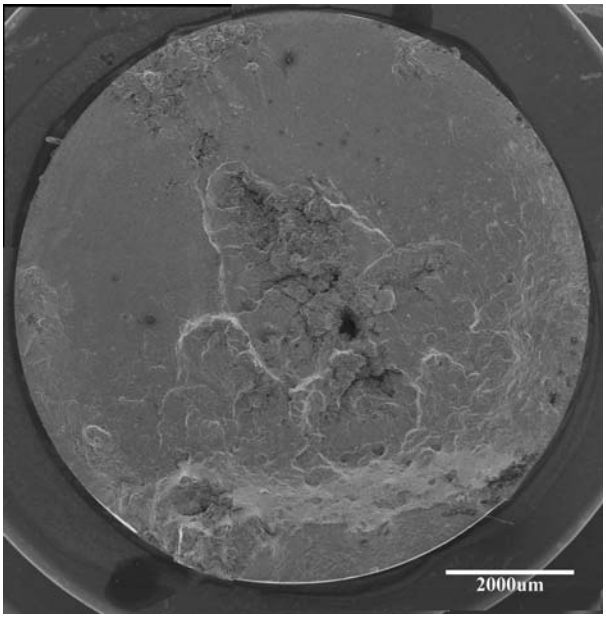

Figure 5.32 - Macroscopic View of a Straight Cylinder Specimen Fracture Surface, S_a = 196 MPa (Specimen B7)

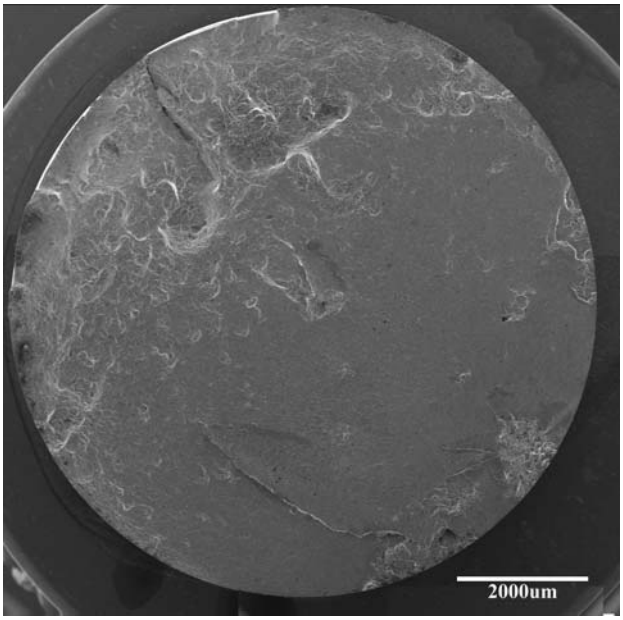

Figure 5.33 - Macroscopic View of a Straight Cylinder Specimen Fracture Surface, S_a = 147 MPa (Specimen G4)

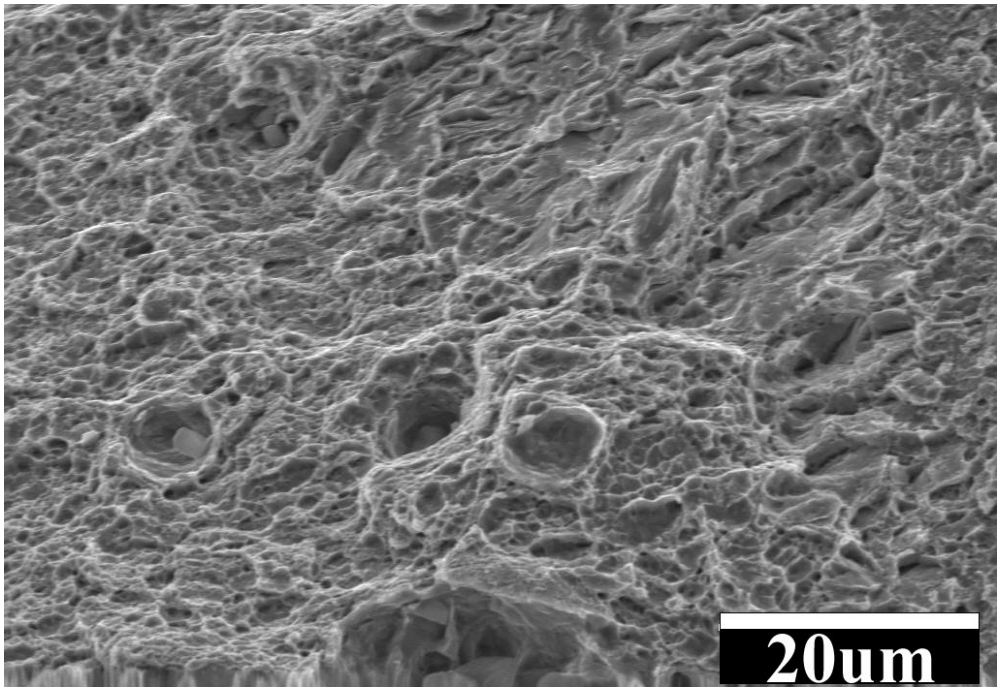

Figure 5.34 - Microscopic View of the Final Fracture Region on a Straight Cylinder Specimen Fracture Surface, S_a = 196 MPa (Specimen B7)

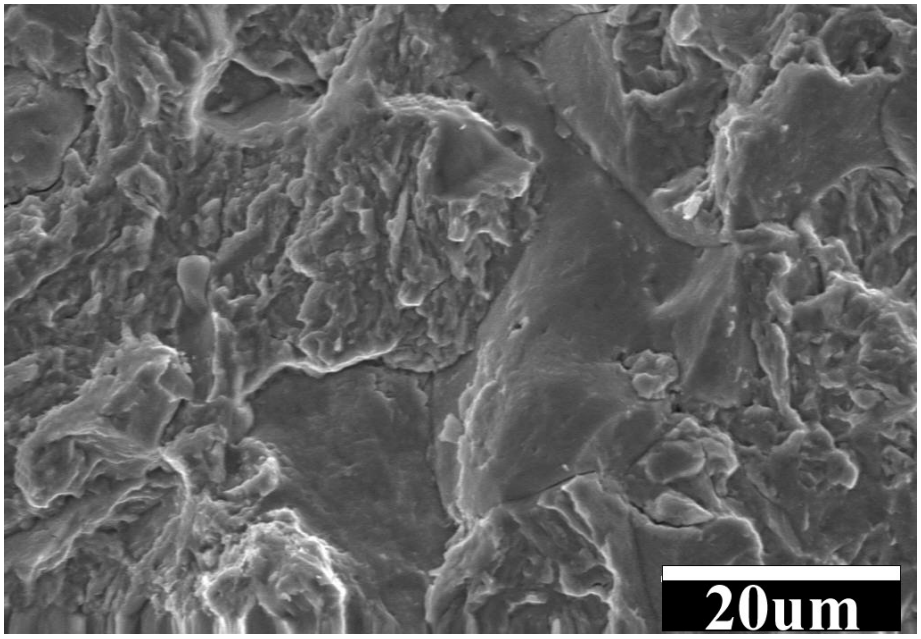

Figure 5.35 - Microscopic View of the FCG Region on a Straight Cylinder Specimen Fracture Surface, S_a = 196 MPa (Specimen B7)

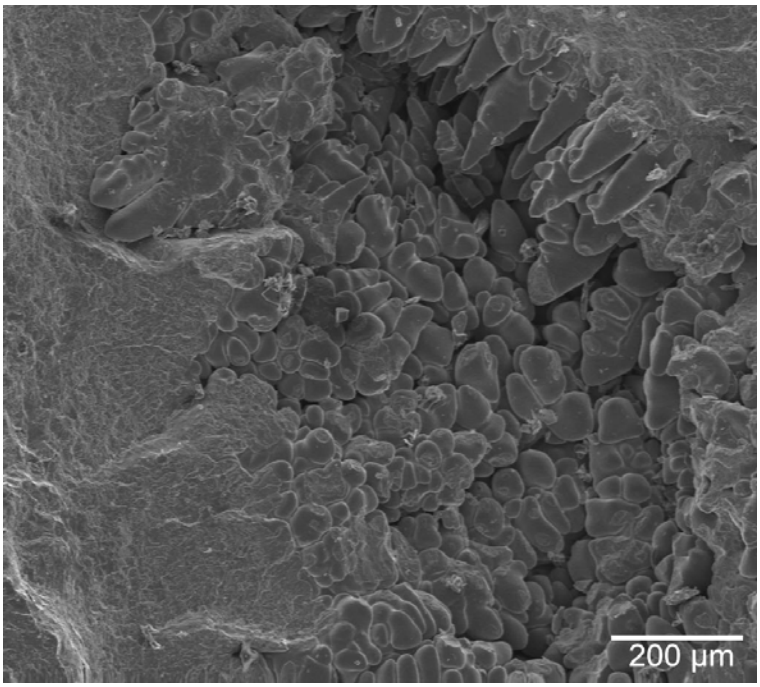

Figure 5.36 - Dendrite Formation on a Straight Cylinder Specimen, S_a = 196 MPa (Specimen B7)

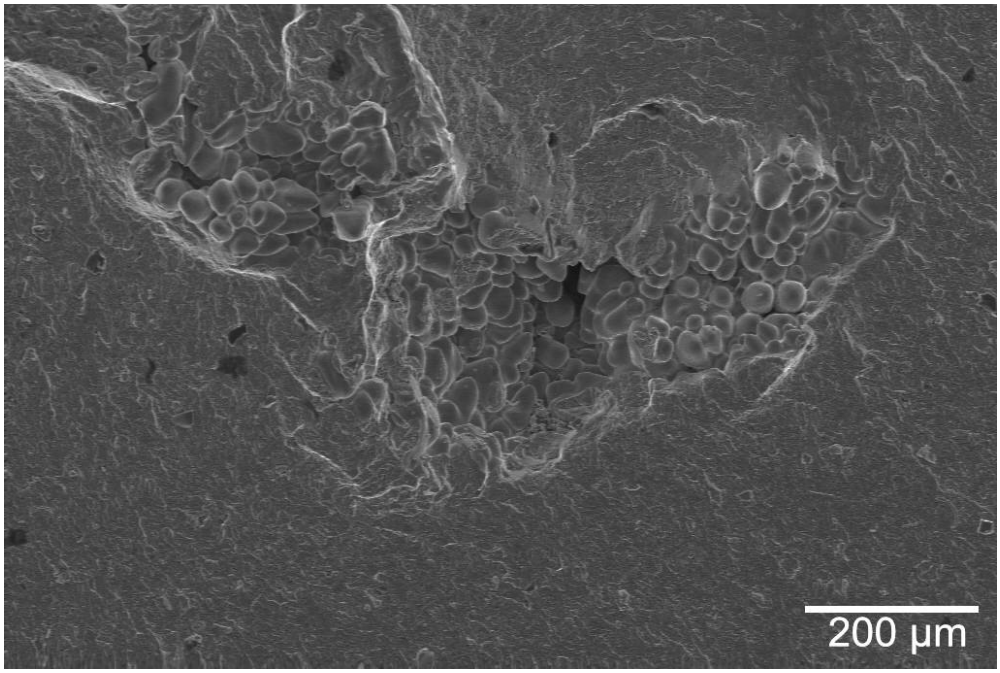

Figure 5.37 - Dendrite Formation on a Straight Cylinder Specimen, S_a = 147 MPa (Specimen G4)

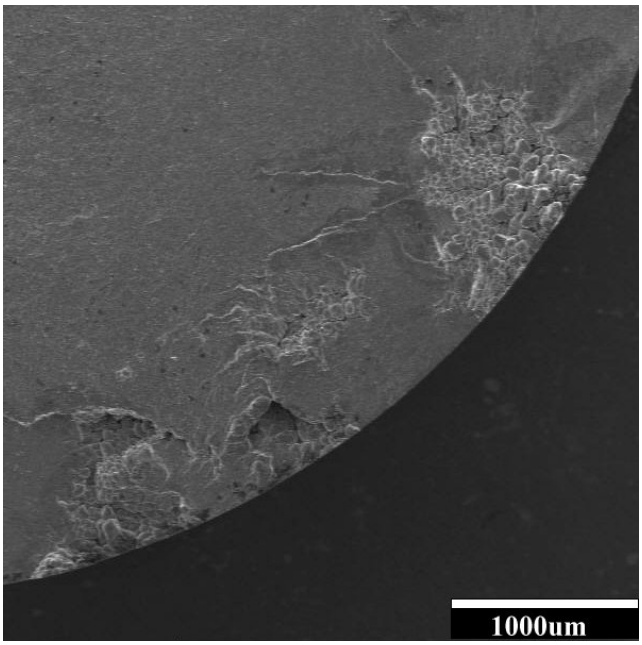

Figure 5.38 - Fatigue Crack Initiation Site on a Straight Cylinder Specimen, S_a = 147 MPa (Specimen G4)

CHAPTER 6: MICROSCOPY

6.1 Microscopy Procedure

In the previous research done by Kyle Sigl in 2002[2], testing material originally thought to be sound, showed evidence of microporosity. From the previous chapter on fractography, porosity was observed on the fracture surfaces, even in the truncated cone blank specimens. Although the radiographs did not indicate any macroporosity, the occurrence of microporosity in Sigl's cast specimens resulted in the decrease of fatigue life when compared to sound material as shown in Chapter 5. In order to quantify the porosity that contributed to fracture, Kyle Sigl employed grinding to remove the fracture surface on the specimens, and then examining this surface using a SEM. Similar methods were used on selected specimens for this research. This method is based on the assumption that a specimen will fracture in an area of high porosity. If the porosity is distributed locally in the volume of the fracture, grinding down the fractured surface can reveal the representative porosity that contributed to the fracture per cross-sectional area. Specimens were chosen based on the fractographic analysis and radiographic results. Since porosity was seen on the fracture surfaces in the fractography, it was desirable to estimate the amount of porosity in a uniform cross section. Alternatively if the radiograph showed evidence of macroporosity at the point of fracture it was of interest to determine the amount of porosity at that point. Although not all specimens were used for microscopy analysis, radiographs for each specimen with their indicated fracture zones are available from the University of Iowa Solidification Laboratory upon request.

Preparation of the specimens was accomplished according to ASTM E03 [9]. The standard gives guidelines for grinding and polishing metallographic specimens for use in microscopy, but there is no specific method due to variance in specimen material, hardness, etc. A certain amount of trial and error was used to find a suitable procedure for obtaining a desired finish. The goal of the finish was to reveal porosity in an arbitrary

plane of the specimen; and therefore a completely polished specimen for metallographic analysis was unnecessary.

To remove the fracture surface Al_2O_3 grinding wheels were employed. A 12.7 cm diameter dry stone and a 25.4 cm diameter water wetted stone were both used; however the 12.7 cm wheel seemed to induce excessive heat, so the 25.4 cm wheel was used more frequently as not to alter any of the properties of the surface. The wet stone naturally left a curved surface due to the curvature of the wheel, so the next step used was a rotary table grinder procured from the University of Iowa Material Science Lab. The grinder used abrasive papers of 240, 320, 400, and 600 grit counts. In order to achieve a flat surface, the section of specimen for microscopy was cut from the rest of the specimen. Using a precision band saw, the specimen was clamped in an aluminum jig and a 1-2 cm long section was cut off. Fine grinding was accomplished using the abrasive papers in sequence. Rotating the specimen 45-90º each time the grit increased allowed gauging the depth of the scratches left by each step. The most vital step in this process was the 240 grit grinding process; the flattest possible surface in the shortest amount of time was obtained while the other steps put progressively finer scratches in the specimen.

In Kyle Sigl's procedure [2] the final step in grinding was fine grinding with a 1200 grit abrasive paper. In the current study, a stationary flat plate was used and a 600 grit grinding was repeated along with a 1200 grit grinding. However, under optical 16x magnification there was still visible scratching that was determined to inhibit the detection of porosity. Three different techniques were tried to achieve a better finish. Using a felt rotary wheel and Al_2O_3 buffing compound a mirror finish could be accomplished. A second method involved using a 5 micron alumina slurry. The slurry consisted of Al_2O_3 powder mixed with water where the specimen was ground on a flat glass surface in the slurry. Both of these methods left an undesirable finish for microscopy. The buffing could cover up microporosity while the slurry left an undesirable surface with microscopic facets. The best method employed involved a 2500

grit abrasive paper grinding in a single direction, this left minute scratches that did not affect the detection of pores as small as 2 microns.

The most effective process for obtaining a quality surface for viewing porosity is as follows:

Removal of fracture surface: Al_2O_3 wet stone grinder

Rough Grinding: 240, 320, 400, 600 grit abrasive paper using Rotary Grinder

Fine Grinding: 600, 1200, 2500 grit abrasive paper (wet/dry) used on flat surface

After the surface was acceptable the specimens were mounted onto aluminum stages used for microscopy using a suitable adhesive. They were then cleaned with acetone and alcohol. The Hitachi S-4000 SEM was used along with the IXRF digital imaging system for taking digital images. The lowest magnification possible to obtain was 20x; thus the entire specimen could not be fit into the viewfinder. Using a series of four quadrants, a picture could be assembled to show the entire specimen surface. The composite was rendered using the commercial software PaintShopPro. By adjusting the contrast and brightness, the separate pictures could be combined. To investigate the surface for porosity, the SEM was set to 600-1000x and the surface was scanned slowly. During the scanning process the image sampling rate for the SEM must be set at 60Hz; this reduces the resolution for viewing the surface. For macroporosity, the microscope was centered above spots of interest and pictures were taken at increasing magnification of 20-5000x. For microporosity, the process was more difficult, only clusters of pores could be seen effectively at the scanning rate. Once a cluster was found the magnification was increased to 1500-5000x to examine the porosity. The position of the pores was difficult to identify because there were no landmarks to pinpoint location, however a general vicinity could be determined by measuring the distance to the edge of the specimen. Several representative pictures were taken of these clusters.

6.2 Truncated Cone Blank Specimens

Radiographic analysis for all the truncated cone specimens indicated no macroporosity, however, all the fracture surfaces showed evidence of dendrite formation. Two specimens were chosen from this geometry to examine, one from a monotonic test, and one from a HCF test with a stress amplitude of 588 MPa. Both were used in fractography and yielded similar results, so one was chosen to represent the amount of porosity that developed in the truncated cone geometry. Figure 6.1 shows the specimen radiograph with the indicated fracture zone, and the macroscopic view of the ground fracture surface. The lines drawn in the radiograph indicate the area involved in the fracture, and the arrow shows the approximate point of where the surface was ground back to the shown view. Scratches are visible along the surface but there is no evidence of macroporosity. The casting simulation previously done by The University of Iowa Solidification Laboratory indicated no areas of concentrated porosity and therefore, examination for porosity was conducted over different representative areas. At a magnification of 250x it was possible to detect microporosity. An image is shown at this magnification along with a 1000x image in Figure 6.2. These were taken near the center of the cross section, and are representative of the microporosity found. In this Figure the largest pore can be measured to have a diameter of just less than 5 microns, this is representative of most of the micropores in this specimen. At some locations there was almost no microporosity evident, while at other locations larger micropores were found, but not with the same frequency, and not exceeding 10 microns. Some amount of microporosity is assumed to occur in static casting and cannot be avoided, evidence of this is found in these specimens. This indicates that these specimens were sound.

6.3 Cylinder with Disc Blank Specimens

Macroporosity was radiographically evident in some cases from the cylinder with disc specimens, particularly in specimens from blanks cast with a 5 mm disc. Figure 6.3

shows a macroscopic view of the specimen with the fracture surface ground back and the corresponding radiograph. The arrow indicates the general location of the ground back surface from the radiograph. As in the x-ray, macroporosity is evident in the center of the specimen. This specimen had the most macroporosity of the specimens selected for microscopy, and showed the most radiographic evidence of macroporosity of the cylinder with disc specimens that fractured. The largest pore diameter measured ~0.5 mm, while others measured ~0.25 mm. The affected area spans across 2 mm of the center. Figure 6.4 shows a closer image of the area. The specimen was tested at a cyclic stress amplitude of 392 MPa and a fatigue life of ~43 000 cycles. The life of this specimen was 12% less than the truncated cone stress-life regression line.

It has already been shown through radiography that the thickness of the disc on the casting affected the amount of macroporosity induced. Specimens machined from a blank that had a 3 mm disc showed significantly less macroporosity than those with 5 mm discs. Two specimens from the cylinder with 3 mm discs castings were used to conduct microscopy, one showed some evidence of macroporosity mainly in the fillet area in the radiograph, and the other showed none. Both were tested at a 392 MPa cyclic stress amplitude and had fatigue lives of ~60 000 cycles. Figure 6.5 shows the macroscopic view of one specimen with the corresponding radiograph. Fractography was conducted on this specimen in the previous chapter and the corresponding fractographs appear in Figures 5.21-5.24. Two macroscopic pores appear in Figure 6.5 that correspond to the pores identified in Figures 5.23 and 5.24. Microscopic images of these pores appear in Figure 6.6 at a magnification of 200x. The largest dimension of these pores is ~500 microns and evidence of macroporosity appears in the radiograph. Other specimens with the same casting geometry showed no evidence of macroporosity in the radiograph. An example is shown in Figure 6.7 with the macroscopic view of the ground fracture surface. The macroscopic view agrees with the radiograph showing no macroporosity, and looks similar to the truncated cone specimen in Figure 6.1. The same examination

method used to find microporosity in the truncated cone specimen was used for this specimen. A representative example of the microporosity found in this specimen is shown in Figure 6.8. Most pores found were less than 5 microns, with occasional pores around 10 microns. In comparison with the truncated cone specimen, the pores are not larger, but they seem to have a slightly higher frequency of occurrence. The microporosity was also distributed more evenly over the examined surface.

6.4 Straight Cylinder Blank Specimens

Figure 6.9 shows the ground fracture surface and radiograph of a straight cylinder blank specimen. Radiographically there was macroporosity, and in the fractography the straight cylinder specimens showed extensive dendrite formation. The macroscopic view of this specimen does not contain concentrated amounts of macroporosity, but does show multiple sites of small but visible macroporosity. One of the larger pore sites from the right side of the macroscopic image is shown in Figure 6.10. The largest dimension of the pores is ~200 microns, but the majority are 100 microns or less. This porosity may be indicated on the radiograph, but the majority of the pores seem to have a diameter that may not be resolvable by the x-rays due to the section thickness. Closer inspection of the ground surface reveals microporosity clusters as shown in Figure 6.11. Most of the pores seen microscopically were on the order of at least 5 microns, similar to the other casting geometries, but at an even higher density and slightly larger than observed in the cylinder with disc specimens. Additionally the existence of macroscopic pores is seen across the surface as well. If these clusters are dense enough through a volume, the radiograph may detect the porosity as a field. These porosity fields do not form simple spheres, however the voids may be distributed throughout the section, which reduces the density of the material. A cross-section view may not give an accurate representation of the extent of which the volume is permeated with voids.

6.5 Summary of Microscopy Results

By grinding back the fracture surface, a representative two-dimensional surface involved in the fracture of the specimen was revealed. In conjunction with the radiograph the evidence of macroporosity was confirmed along with the discovery of microporosity. The theoretical limit of resolution for the radiographs was ~200 microns. Any porosity that could not be resolved by x-ray was considered microporosity.

The truncated cone specimens showed no macroporosity in the radiograph, but there was evidence of possible porosity in the fractography due to the formation of dendrites. With the fracture surface ground back it was possible to determine the average size and frequency of the microporosity. The ground surface showed pores with a 5 micron diameter average, with a frequency much less than what Sigl found in the previous study for the sound material. The microporosity evident was considered to be incidental from static casting.

The cylinder with disc specimens showed a wide range of macroporosity in the radiographs ranging from clear to none. Some specimens that showed clear macroporosity in the radiograph were verified by grinding back the fracture surface. The pores in these specimens reached up to 500 microns and were visible at 20x magnification. Other specimens showed a small amount of macroporosity in the radiograph, and were confirmed by the ground surface. Pores that were barely evident on the radiograph measured ~200 microns on the ground surface and were visible at a 20x magnification. Some cylinder with disc specimens showed no macroporosity at all in the radiograph, but the ground surface revealed evidence of microporosity. The average pore diameter measured ~5 microns which was similar to those found in the truncated cone specimens; however their frequency was slightly higher.

The straight cylinder specimens showed clear evidence of macroporosity in the radiographs, but the ground surface revealed only small amounts of macroporosity. There was evidence of microporosity too, with diameters reaching ~20 microns at higher

densities. The amount of macroporosity shown in the radiograph was not seen in the same form as it was seen in the cylinder with disc specimens. Rather, it is theorized that the density of pores was large enough show evidence of macroporosity in the radiograph without having contiguous pores that would be visible macroscopically.

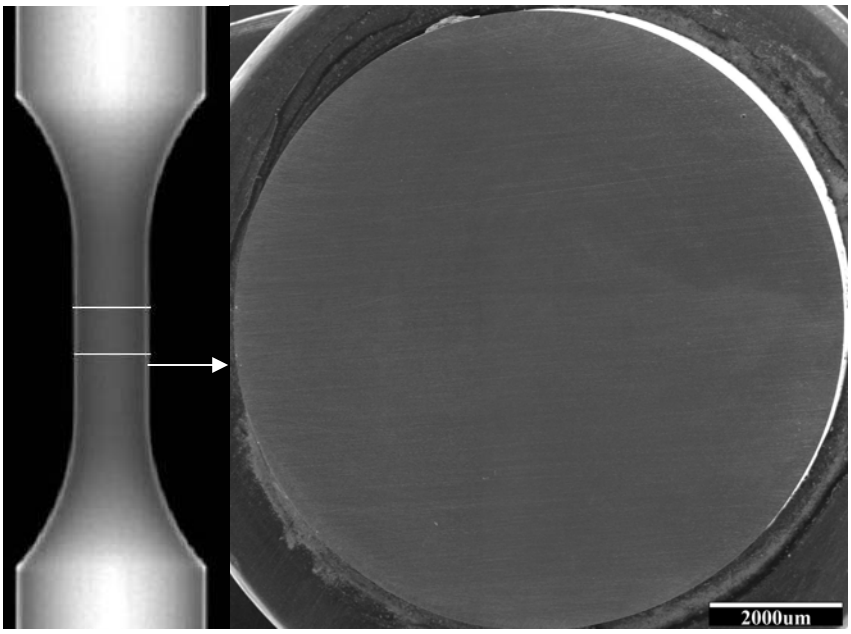

Figure 6.1 - Radiograph with Indicated Fracture Zone and a Macroscopic View of a Truncated Cone Specimen with the Fracture Surface Ground Back (Specimen A6)

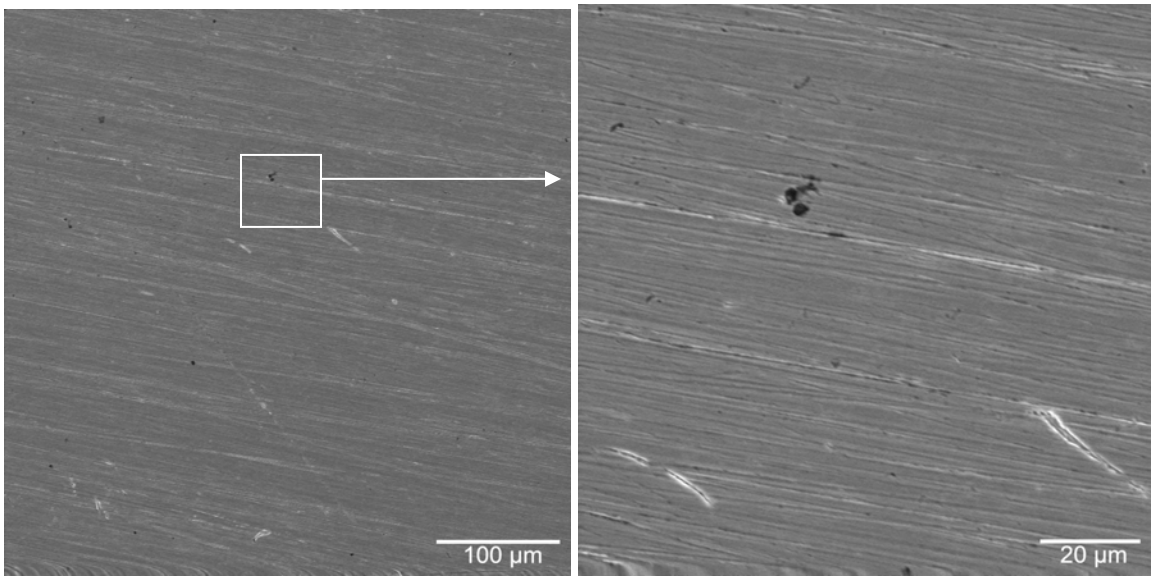

Figure 6.2 - 250x and 1000x Images of Representative Microporosity on a Ground Fracture Surface of a Truncated Cone Specimen (Specimen A6)

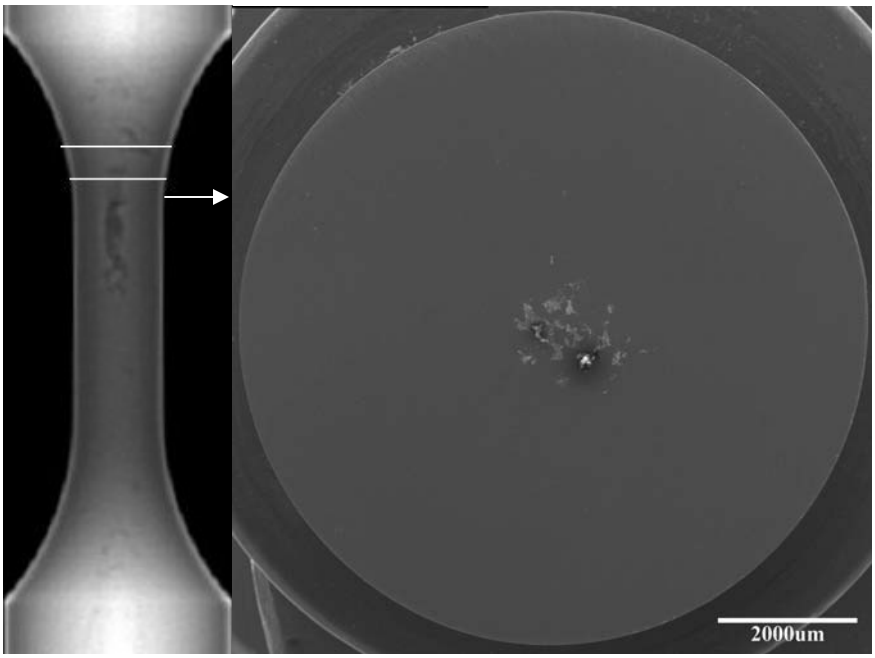

Figure 6.3 - Radiograph with Indicated Fracture Zone and a Macroscopic View of a Cylinder with 5 mm Disc Specimen with the Fracture Surface Ground Back (Specimen C6)

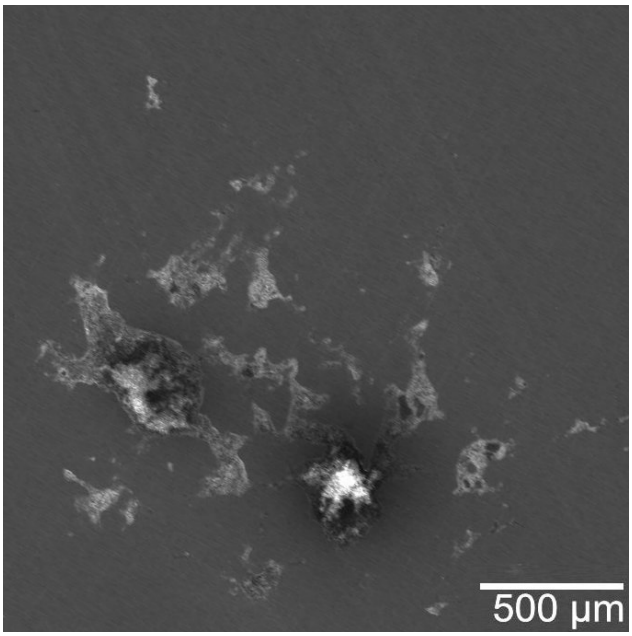

Figure 6.4 - Magnified View of Macroporosity in a Cylinder with 5 mm Disc Specimen with the Fracture Surface Ground Back (Specimen C6)

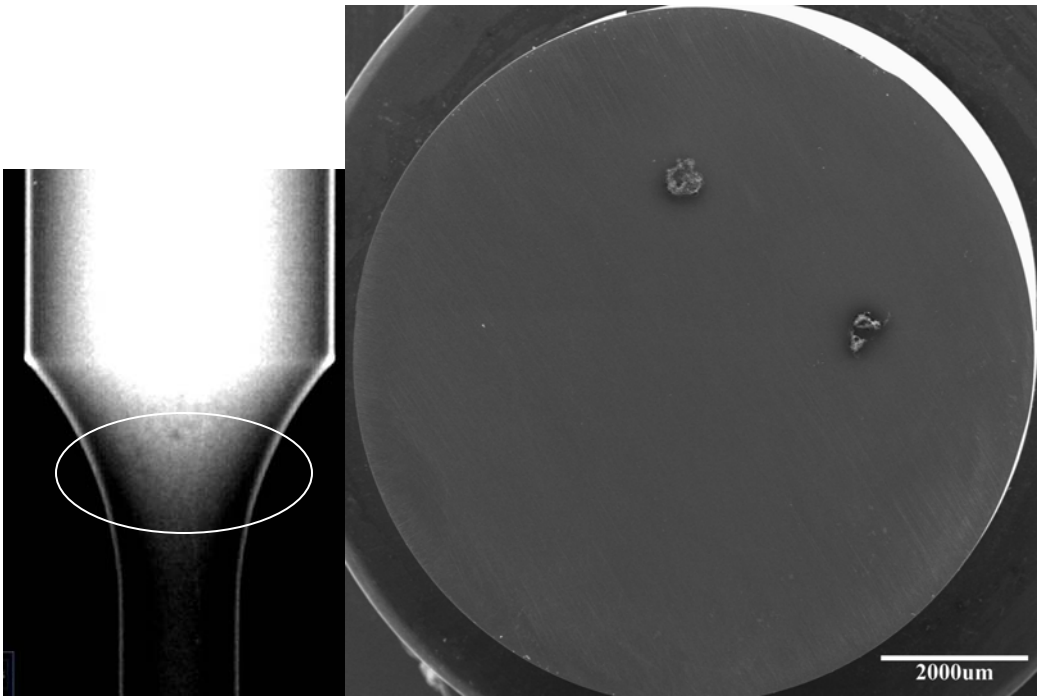

Figure 6.5 - Radiograph with Indicated Porosity Zone and a Macroscopic View of a Cylinder with 3 mm Disc Specimen with the Fracture Surface Ground Back (Specimen H5)

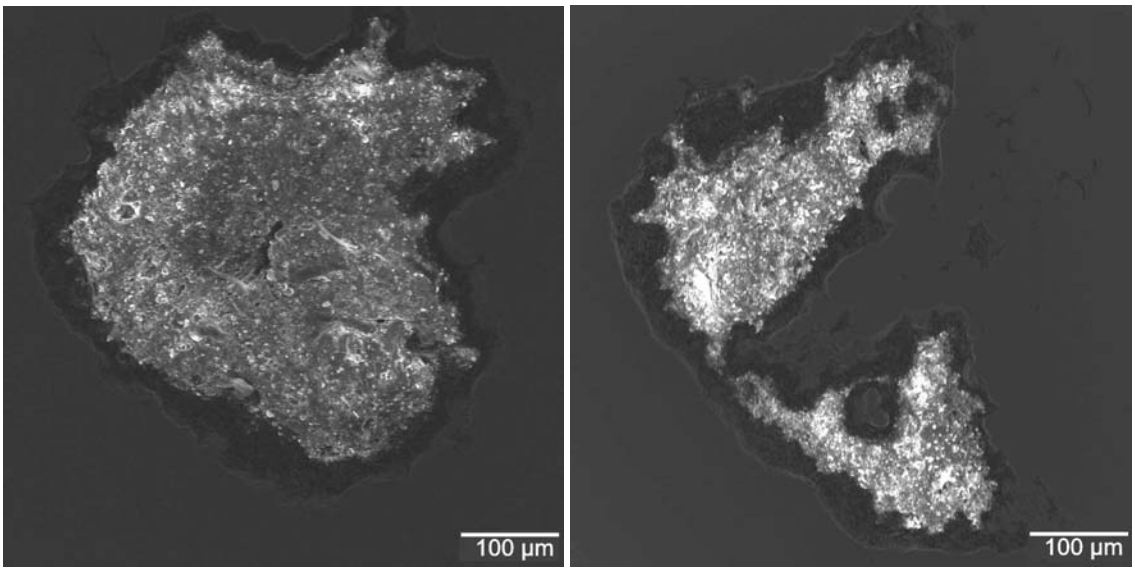

Figure 6.6 - Magnified View of Macroporosity in a Cylinder with 3 mm Disc Specimen with the Fracture Surface Ground Back (Specimen H5)

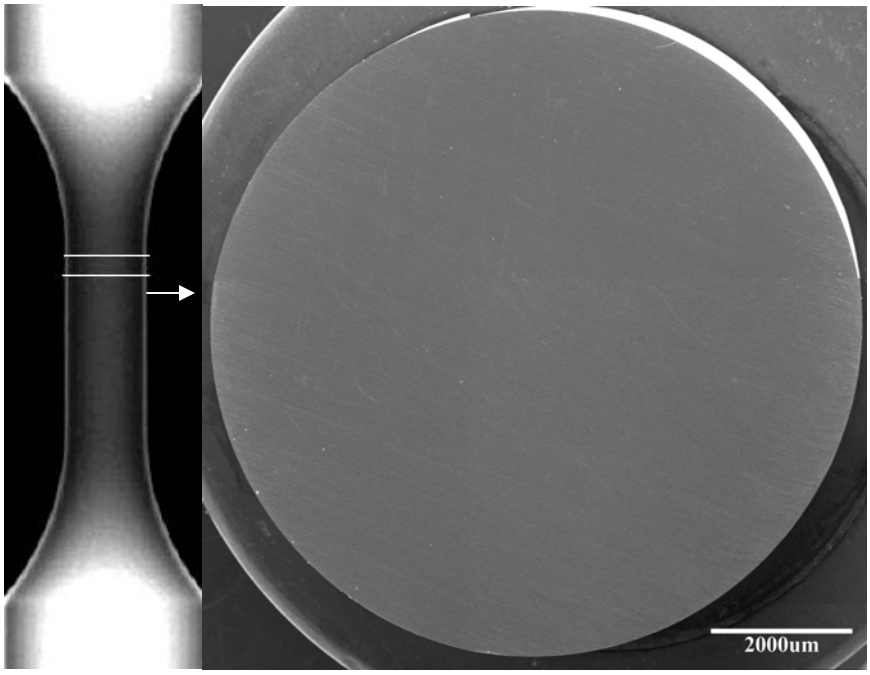

Figure 6.7 - Radiograph with Indicated Fracture Zone and a Macroscopic View of a Cylinder with 3 mm Disc Specimen with the Fracture Surface Ground Back (Specimen E5)

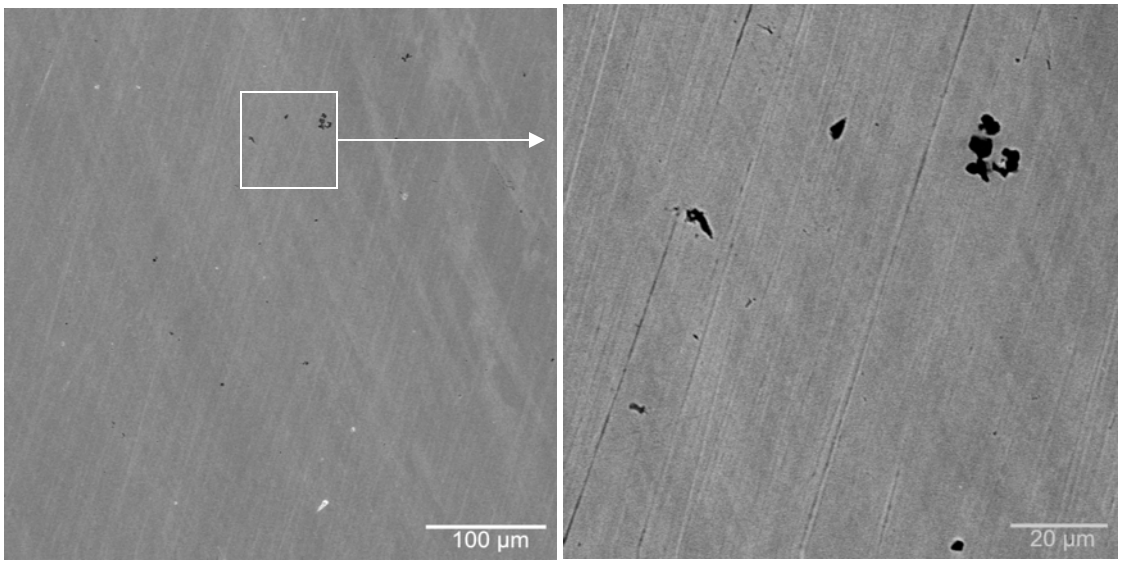

Figure 6.8 - 250x and 1000x Images of Representative Microporosity on a Ground Fracture Surface of a Cylinder with 3 mm Disc Specimen (Specimen E5)

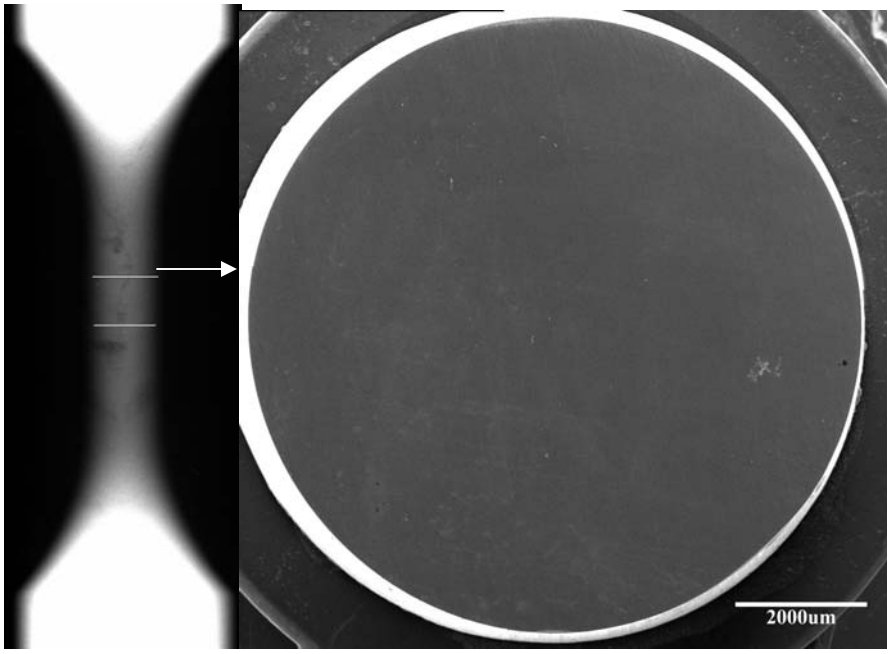

Figure 6.9 - Radiograph with Indicated Fracture Zone and a Macroscopic View of a Straight Cylinder Specimen with the Fracture Surface Ground Back (Specimen B7)

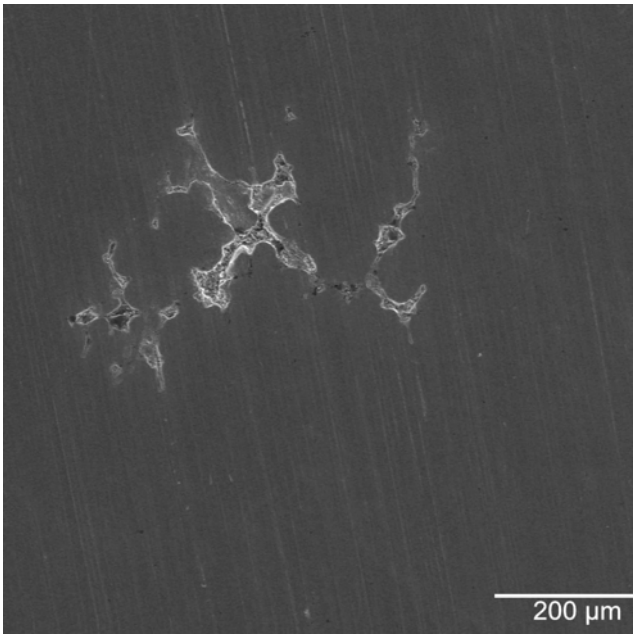

Figure 6.10 - Magnified View of Macroporosity in a Straight Cylinder Specimen with the Fracture Surface Ground Back (Specimen B7)

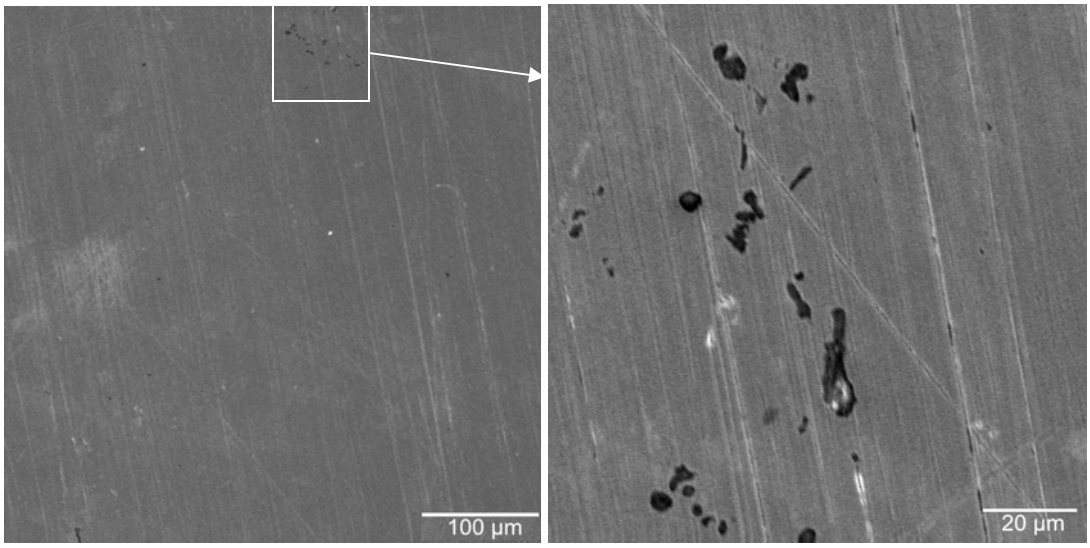

Figure 6.11 - 250x and 1000x Images of Representative Microporosity on a Ground Fracture Surface of a Straight Cylinder Specimen (Specimen B7)

CHAPTER 7: DISCUSSION OF RESULTS

7.1 Comparison of Monotonic Properties

The monotonic results of the truncated cone specimens were supposed to closely resemble the results of the keel block specimens tested for the SFSA [3] in 1983. A keel block is regarded as the most reliable method for obtaining sections of sound material in a casting. Kyle Sigl used specimens machined from castings that resembled an oversized specimen. The Sigl specimens were, however, found to have significant microporosity that affected some monotonic and fatigue properties [2]. The truncated cones were designed to have a strong temperature gradient that was supposed to minimize the formation of macro and microporosity. Cast steels, regardless, will often contain some porosity. Wrought steels cast as ingots are worked into their final form; this manipulation of the material removes most porosity, especially at the surface where the material undergoes the most work. Comparison of the truncated cone specimens to the SFSA keel block specimens and to the Sigl microporosity specimens are used to determine the relative soundness of the truncated cone.

The ultimate tensile strength, S_u, and modulus of elasticity, E, are similar between the three groups, but Sigl has shown that these values can be close even in the presence of microporosity [2]. The yield strength, S_y, is 14% higher on the truncated cone specimens than the value found for the SFSA study, but only 3% different from the Sigl specimens. The higher S_y with a similar S_u could indicate less ductility, and Sigl found that a lack of ductility can be a sign of microporosity. Percent reduction of area, %RA, is an indicator of the ductility of a material, where Sigl saw only ¼ of the %RA measured in the SFSA study, while the truncated cone specimens saw on average ½ of the SFSA value. The differences between S_y and %RA for the truncated cone specimens in comparison to the SFSA properties may be an indicator of microporosity, but may instead be slight differences in heat treatment, chemistry, or testing procedure. Heat treatment between the

three groups were supposed to be identical, yet there is some room for variance, such as the water quenching, which had affects on the current study more so than the previous ones. The chemistry for the steels all were within the specifications for manganese and carbon, with respect to 8630 wrought steel. For castings the amount of silicone is increased to aid in fluidity, and other elements such as chromium, molybdenum, and nickel are considered incidental and can vary by a certain percentage. For all three studies the steel falls in the specification of 8630 cast steel, but there are differences in the chemistry.

7.2 Comparison of Cyclic/Fatigue Properties

Using the cyclic and fatigue properties, the three studies can be compared to further determine their similarities and differences. The cyclic stress-strain curve for the truncated cone specimens showed some inconsistent trends. The peak stress values were lower for some of the higher strain amplitude specimens. This is shown in the hysteresis loops in Figure 4.4. This was most likely due to the inability of the specimens to reach a steady stress amplitude during strain controlled fatigue testing. Figure 4.3 demonstrated how higher strain amplitude specimens continued to have falling stresses over their lives. Initially there is evidence of cycle softening, but the stress never obtained a steady value for any portion of the life. The lower strain amplitude specimens from 0.005-0.0035 exhibit somewhat more consistent behavior, but cycle harden initially instead. These results prompted the use of an incremental fatigue test specimen. Although the specimen did not have the higher strain amplitudes of 0.01 and 0.008, it still exhibited the same trends seen in the companion method. The highest strain amplitude 0.006 had a lower peak stress than the next lowest amplitude. This is demonstrated in the hysteresis loops for the incremental specimen, which are shown in Figure 4.5.

Comparing the cyclic stress-strain properties for the truncated cone specimens to Sigl's and the SFSA results show some similarities and differences. The fatigue strength,

S_f at $2x10^6$ cycles, for the truncated cone specimens is 28% higher than the value found by Sigl, but is still 29% lower than the benchmark value of the SFSA specimens. The fatigue strength can be dependent on the ability to resist crack initiation. The truncated cone specimens were designed with larger dimensions than the previous two studies, so if the amount of microporosity was consistent with the keel block specimens there would have been a greater ability to develop fatigue cracks due to the increased surface area of the larger specimen. Sigl's specimens had a lower S_f due to microporosity; the pores acted as a local stress riser and initiated fatigue crack growth. The cyclic strength coefficient, K', and cyclic strain hardening exponent, n', for the truncated cone specimens were closer to the values found for the keel block specimens than for Sigl's microporous specimens. Using Equation 7.1 these values can be used to calculate a representative cyclic stress-strain curve for each study.

$$\varepsilon_a = \frac{\sigma_a}{E} + \left(\frac{\sigma_a}{K'}\right)^{1/n'} \tag{7.1}$$

Comparison of the cyclic stress-strain behavior of the different studies showed that the SFSA specimens tended to cycle soften more rapidly than the other two studies. The cyclic yield strength, S_y', is dependent on this behavior, and was higher for both the truncated cone specimens and Sigl's specimens by more than 25%, when compared to the averaged benchmark value for the sound material from the SFSA study. This is consistent with the increased S_y found for the monotonic values. The cyclic behavior is not conclusive of the relative soundness of the material. Cyclic softening and hardening is controlled by the microstructure of the material. Although micropores have considerable impact on the microstructure the amount of micropores seen in the microscopy is minimal. Furthermore the size of the micropores is small enough that the stress concentration in fatigue would have negligible effects on the life. Grain sizes and

crystalline structure is more influential for cyclic behavior, and is dependent on factors such as heat treatment and chemistry.

Using a strain-life comparison the fatigue behaviors can be compared. The fatigue ductility exponent, c, and the fatigue ductility coefficient, ε_f' are indicators of the amount of plastic strain the material exhibits during cycling. Likewise the fatigue strength exponent, b, and the fatigue strength coefficient, σ_f', are indicators of the elastic strain exhibited. These values can be used to plot curves that represent the strain-life behavior of the material. The intersection of these curves is called the transition fatigue life and indicates when the deformation is mainly elastic or plastic. The keel block has an early intersection of the plastic and elastic strain curves, while the truncated cone specimens and Sigl's microporous specimens elastic and plastic strain curves never intersect. This indicates that specimens in this current study and Sigl's specimens are dominated by elastic deformation, and have less plasticity. This is consistent with the lower ductility and high S_y'. The combination of these lines represents the complete strain-life behavior of the material. Figure 4.8 shows a comparison of the truncated cone specimens, the SFSA keel block specimens, and Sigl's microporous specimens. The microporous specimens clearly fall lower than the keel block specimens, but the truncated cone specimens and keel block specimens have similar behavior up to ~30 000 reversals. The two curves deviate after that point which is primarily dependent on elastic behavior. This effect may again be attributed to the heat treatment, chemistry, testing accuracy, or the size difference. It can be concluded from the strain-life curves, that the truncated cone specimens come much closer to representing sound material than the specimens Sigl tested.

Further evidence to show that the truncated cone specimens were sound was through the use of fractography and microscopy. The fractography for the truncated cone specimens revealed dendrite formation in the fracture surface, which may have been a sign of porosity. However, the amount and size could not be measured since the cross

sectional area was too irregular. The microscopy procedure was developed to show a representative amount of porosity that caused fracture. After grinding the fracture surface back, a two-dimensional representation of the porosity was revealed near the fracture zone. The porosity that was found was all microscopic which is validated by the radiographs. The average size of a pore was found to be ~5 microns with very few present. Sigl saw pores at a slightly larger size with many more present. Qualitatively the amount of microporosity found in Sigl's research was much higher than seen in the truncated cone specimens. The microporosity seen in the truncated cone specimens was concluded as being incidental porosity that occurs naturally in casting, and the truncated cone specimen can be considered basically sound material.

7.3 Stress-Life Comparison of the Cylinder with Disc Specimens to the Truncated Cone Specimens

From the strain-life comparison with the SFSA keel block specimens, and the fractography and microscopy it was reasonable to assume the truncated cone specimens represent "sound" material. The fatigue data from the truncated cone specimens were converted to represent a stress-life curve. This was done to directly compare the cylinder with disc specimen results to the truncated cone specimen results. The cylinder with disc specimen data were superimposed onto this curve to determine the effect of the porosity on the fatigue life. It was unexpected to see the scattered data (open and solid squares) fall close to the sound material curve as shown in Figure 4.10. Furthermore the size of the disc had little effect on the fatigue life when compared to each other. The lives at the ~600 MPa stress amplitude had a small amount of scatter, and an average life greater than the sound regression line. The lives at the ~400 MPa stress amplitude had a greater amount of scatter with an average life that fell very close to the sound data. The 5 mm disc specimens had greater evidence of macroporosity in the radiographs, yet the lives of those specimens were, on average, close to the specimens machined from 3 and 4 mm

disc blanks. At the ~200 MPa level all the disc specimens, except one, achieved the run-out criterion of $2x10^6$ cycles. The analysis of the stress-life data for these specimens indicates that the induced porosity in the cylinder with disc specimen did not significantly affect the fatigue life.

Fractography and microscopy of the cylinder with disc specimens revealed an increase of dendrite formation and some macroporosity. The ground fracture surfaces used in microscopy revealed macroporosity on some specimens that was on the order of ~ 200 to 500 microns. The specimens also showed limited amounts of microporosity which were similar to that seen in the truncated cone specimens. The simulation of the castings produced by the University of Iowa Solidification Laboratory did predict the macroporosity that occurred and was confirmed by radiography. However the fatigue life of the cylinder with disc specimens was unexpected because it seemed that the predicted porosity did not affect the fatigue life. Closer analysis of the simulation showed that both macroporosity and microporosity of the cylinder with disc, casting focused the porosity above and below the disc. At the center of the disc the material was predicted to be close to as sound as the truncated cone specimens. This center portion was machined into the reduced test section of the specimen. The specimen radiographs confirmed this by showing macroporosity in the fillets, but not always extending into the test section. The test section was basically sound material with macroporosity outside in the fillets. This would also explain the fracture of some of these specimens outside the test section in the fillets. The microscopy results verified that the total amount of porosity in the cylinder with disc specimen at the fracture zone was relatively minimal, even for the specimens that showed macroporosity. The reason the fatigue life was close to that of the sound fatigue life was because the material in the test section was basically sound.

7.4 Stress-Life Comparison of Straight Cylinder Specimens to the Truncated Cone Specimens

Using the same sound regression curve from the truncated cone specimens the data from the straight cylinder specimens were superimposed on the plot shown in Figure 4.10. The lives for the straight cylinders were significantly less than the sound curve as shown by the open triangles and the dashed regression line in Figure 4.10. Generally their lives were close to an order of magnitude less, and the run-out criterion of $2x10^6$ cycles was not achieved at the ~200 MPa stress amplitude. Two lower stress amplitudes were tested before run-out was achieved. The behavior of the straight cylinder specimens have a more similar behavior to the microporous specimens that were tested by Sigl. However in the radiographs there was evidence of macroporosity, which was not present in Sigl's microporous specimens. The radiographs for the straight cylinder blanks contain more macroporosity in the reduced test section than the cylinder with disc specimens.

The fractography of the straight cylinder specimens showed more extensive dendrite formation than found in any of the other types of casting geometry. This shows that the volume of the pores was probably larger than in any of the other specimens. Grinding back the fracture surface did not uncover as much macroporosity as anticipated. There were signs that the porosity was not localized to the center of the specimen, rather it was distributed throughout the specimen test section. The microporosity was also larger and more frequent. The total amount of porosity seen in the ground back fracture surface is qualitatively less than the macroporosity seen in some of the cylinder with disc specimens; however the fatigue lives for the straight cylinder specimens fall consistently less than any of the other specimens. This could be due to the more consistent distribution of porosity throughout the test section. The simulations showed that the center of the straight cylinder casting blank had the highest amount of porosity, and was spread throughout the length of the casting. Radiographs showed macroporosity in the entire specimen test section lengths for the straight cylinders. The cylinder with disc specimens

occasionally showed macroporosity in the test section, and only when the macroporosity was severe in the fillets. The porosity that was induced in the straight cylinder specimens affected the fatigue life because of the consistency of porosity in the test section. This is also consistent with the results of Sigl's testing, showing that microporosity can affect the fatigue life without consuming a large percentage of volume.

7.5 Modulus of Elasticity Results

It has been shown that the modulus of elasticity, E, can somewhat be used as a corrector for the true stress in porous specimens, as was done in a study published by Sigl et al [4]. The stress measured during testing is calculated from the measured load divided over a nominal cross sectional area. If the nominal area is affected by porosity the calculated stress will not be the true stress acting over the test section. The measured modulus of elasticity for porous material based on the nominal cross section is usually lower than that found in sound material. A more representative true stress (S_{calc}) can be derived using the ratio of the sound monotonic modulus of elasticity (E_s) and the measured modulus of elasticity (E_m) from each individual specimen, multiplied by the nominal stress (S_m), as found in Equation 7.2:

$$S_{calc} = S_m \frac{E_s}{E_m} \tag{7.2}$$

Using this corrector a linear trend between the measured modulus and the true stress has been hypothesized. Based on this representative stress the area affected by porosity can theoretically be back calculated.

Individual specimen modulus of elasticity is listed for each specimen in Tables 4.3-4.7. The statistical mean, median, and standard deviation of the modulus of elasticity for the different casting blanks is shown in Table 4.8. When compared to the monotonic modulus found in Table 4.1 the difference is negligible for the cylinder with disc specimens. When the theory was applied to the data in the current study the stress

correction was virtually unity and had negligible affect on the stress amplitude. The modulus of elasticity for the straight cylinder specimens had values similar to the monotonic specimens on an average; however the standard deviation had a much higher value. When the correction is applied to the straight cylinder specimens some stress amplitudes are increased, but most are unaffected, including most of the outlier specimens. The specimens that are affected do not have an increase of stress amplitudes to match the sound regression line. This was also found in the Sigl et al study, where it could help in separating groups with similar moduli, but it could not completely account for the stress amplitude difference.

Another drawback of this technique lies in the assumption that the sound modulus of elasticity is the true value. The moduli for the HCF tests are consistently higher than the monotonic value, including the truncated cone HCF values. The LCF modulus of elasticity values, however, have greater scatter, including lower than monotonic values. During fatigue testing the specimen modulus can change due to cycle hardening or softening. In this particular study the material has shown to do both in different conditions. Figure 4.3 shows LCF specimens tend to cycle soften at strain amplitudes greater than 0.005, and tend to cycle harden then soften at strain amplitudes of 0.005 and 0.004. For strain amplitudes 0.0035 and lower there is evidence of cycle hardening, even though the effect should be negligible due to totally elastic behavior. Nonetheless the moduli for the majority of the specimens had slightly higher values than the monotonic value. The method has better application for gross section loss due to porosity, but for this study the reduction in modulus of elasticity is not apparent for the amount porosity encountered.

7.6 Comparison of Current Results to Sigl's Results

Although the cylinder with disc specimens did not show significant fatigue life differences from the truncated cone specimens, the straight cylinder specimens had

evidence of macroporosity, and significant fatigue life difference. The elimination of the large ratio of pores to test section area that occurred in Sigl's specimens was accomplished for the current research. Originally the purpose of the research done by Sigl was to determine the effects of porosity on the fatigue life of 8630 cast steel with comparison to sound material. The material he thought would be sound ended up containing microporosity that affected the fatigue properties. The comparison of Sigl's macroporous specimens to the microporous specimens did not yield the results that were hoped, because of the significantly reduced fatigue resistance of the macroporous specimens.

Figure 4.11 shows the results of all the current study's specimens, and Sigl's micro and macroporous specimens. The microporous specimens tested by Sigl has a regression line that follows the two current data regression lines. However it is lower than the current research sound regression line. Additionally the straight cylinder specimens tested in the current research have lower life at similar stress levels than Sigl's microporous specimens. This is consistent with the radiographic evidence, where the straight cylinder specimens show macroporosity. Sigl's microporous specimens appear radiographically sound, and therefore the microporous specimens should have greater life.

The macroporous specimens tested by Sigl were tested at significantly lower stress amplitudes than any other specimen group because of the excessive amounts of macroporosity. Ultimately the comparison of Sigl's porous material fatigue life was not as meaningful as hoped from Sigl's study due to these results. The current research accomplished casting a relatively sound specimen with comparable fatigue results to the sound material from the SFSA study, and showed better fatigue properties than Sigl's microporous specimens. Furthermore the straight cylinder specimens showed macroporosity and had fatigue lives that were less than the sound material. This was possible due to the increased specimen size and less percentage of porosity than what Sigl

saw in his macroporous specimens. The straight cylinder specimens showed macroporosity in the radiographs, and have lower fatigue lives than the microporous specimens tested by Sigl. However the truncated cone specimens have higher fatigue lives than the microporous specimens, and have less porosity than the Sigl microporous specimens. Based on the various levels of porosity found in the current study and of Sigl's study a qualitative correlation can be shown between the amount and/or size of porosity to fatigue life.

CHAPTER 8: SUMMARY, CONCLUSIONS, AND RECOMMENDATIONS

8.1 Summary and Conclusions

1. Truncated cone blanks were designed to have a strong temperature gradient to minimize the formation of any porosity. Specimens machined from these blanks were to simulate the sound material obtained from a keel block casting.
2. Monotonic properties were obtained for the truncated cone specimens and compared to the properties found in studies by Sigl [2] and the SFSA [3], these are found in Table 4.1. The properties for the truncated cone specimens such as ultimate tensile strength (S_u), tensile yield strength (S_y) and modulus of elasticity (E) were similar to the other studies; however there was less ductility found than the sound material in the SFSA study.
3. Cyclic properties of the truncated cone specimens were calculated and compared to the same two studies, and are found in Table 4.2. Fatigue strength (S_f) was 29% lower than the SFSA benchmark, but was significantly increased from Sigl's value. Both the truncated cone specimens and the specimens from Sigl's study showed at least a 20% increase in cyclic yield, (S_y'), strength over the SFSA data. This was consistent with the lower amount of ductility of the truncated cone specimens compared to the SFSA results. The cyclic stress-strain behavior of the SFSA sound material showed more cyclic softening than the other two studies.
4. The differences in the monotonic and cyclic values can be primarily attributed to slight variations in heat treatment and chemistry. Overall the cyclic stress-strain behavior is not conclusive of the relative soundness of the material.
5. The truncated cone specimens combined elastic and plastic curve showed a trend that was similar to the keel block specimens tested for the SFSA study.

The specimens tested by Sigl that were found to be microporous, showed a definite difference in the comparison. The conclusion from this comparison shows the truncated cones were sound castings.

6. Microscopy of the truncated specimens also validated the relative soundness. Although pores were found in the cross section, they were on average ~5 microns and were spaced much farther apart than the pores found in Sigl's microporous specimens. Since the pore size was small and the spacing was considerably more than found in Sigl's microporous specimens the effect on the fatigue was determined to be negligible.
7. The micropores found in the truncated cone specimens were considered incidental from casting. The elimination of all porosity from static casting is virtually impossible.
8. The fatigue lives of the cylinder with discs did not have significant differences from that of the truncated cones specimens. The thickness of the disc also had no effect on the fatigue life. Specimens with the 5 mm disc showed no difference in fatigue life when compared to the 3 and 4 mm disc specimens.
9. Radiography of the cylinder with disc specimens showed indications of macroporosity, but the majority of macroporosity was found outside the test section in the fillets. Examination using microscopy behind the fracture surface revealed some macroporosity, along with indications of microporosity. Inspection of casting simulation revealed the porosity was focused outside the center of the casting, so that the bulk of the porosity formed where the fillets were machined.
10. The test sections of the cylinder with disc specimens had similar amounts of porosity as the truncated cone specimens, and were therefore basically sound. Although porosity was found, the majority was located outside the test

section; therefore the cylinder with disc specimens had results which reflected the sound material.

11. On average the fatigue lives of the straight cylinder specimens were decreased by a factor of 10 compared to the truncated cone specimens.
12. Fractography showed extensive dendrite formation in the straight cylinder specimens that indicated large pores. Microscopy did not show gross cross sectional area loss to pores, but revealed an even distribution of small macroporosity and extensive microporosity formation.
13. The even distribution of porosity through the test section of the straight cylinder specimens resulted in a definite decrease in fatigue life. This result is consistent with the findings of Sigl's microporous specimens that show microporosity can significantly affect fatigue life without consuming a large percentage of volume.
14. Comparison of results of the current research and Sigl's results show that the various amounts of porosity can significantly affect fatigue life. The truncated cone and cylinder with disc specimens have longer fatigue lives than Sigl's microporous specimens, which have longer fatigue lives than the straight cylinder specimens that contain macroporosity. Sigl's macroporous specimens showed excessive amounts of macroporosity and had significantly shorter fatigue lives.

8.2 Recommendations

1. A detailed examination of the straight cylinder specimen radiographs should be performed the estimate the amount of macroporosity in the test section. A quantitative examination using microscopy or another method should be used to estimate the amount of microporosity. Using this information a comparison could be made to Sigl's microporous specimens.

2. Revisions should be made to the casting blank, based on the truncated cone and straight cylinder configurations, to consistently generate differing amounts of porosity at the center of the blank. Specimens can be axially tested for fatigue with varying amounts of porosity.

REFERENCES

1. Lankford, W. T., Samways, N. L., Craven, R. F., The Making, Shaping and Treating of Steel, 10th Edition, Hebrick & Held, Pittsburgh, PA, 1985.

2. Sigl, K. M., The Influence of Porosity on the Fatigue Behavior of 8630 Cast Steel, Masters Thesis The University of Iowa, 2003. Iowa City: UI, 2003. T2003 .S587.

3. Stephens, R.I., Fatigue and Fracture Toughness of Five Carbon or Low Alloy Cast Steels at Room or Low Climatic Temperatures. Carbon and Low Alloy Technical Research Committee, Steel Founders' Society of America, Des Plaines, IL, 1982.

4. Sigl, K. M., Hardin, R. A., Stephens, R. I., Beckermann, C., "Fatigue of 8630 Cast Steel in the Presence of Porosity", International Journal of Cast Metals Research, Vol. 17, No. 3, 2004, pp. 130-146.

5. Standard E18. "Verifications of Machines for Rockwell Hardness and Rockwell Superficial Hardness Testing" 2004 Annual Book of ASTM Standards, Vol. 03.01, American Society of Testing and Materials, West Conshohocken, PA, 2004, pp. 138-149.

6. Steel Founders' Society of America, Steel Castings Handbook, 6th ed., Steel Founders' Society of America, Materials Park, OH, 1995.

7. Standard E606. "Standard Practice for Strain-Controlled Testing" 2004 Annual Book of ASTM Standards, Vol. 03.01, American Society of Testing and Materials, West Conshohocken, PA, 2004, pp. 592-606.

8. Standard E1030. "Standard Test Method for Radiographic Examination of Metallic Castings" 2004 Annual Book of ASTM Standards, Vol. 03.03, American Society of Testing and Materials, West Conshohocken, PA, 2000, pp. 479-489.

9. Standard E3. "Standard Guide for Preparation of Metallographic Specimens." 2004 Annual Book of ASTM Standards, Vol. 03.01, American Society of Testing and Materials, West Conshohocken, PA, 2004, pp. 1-12.